






Multifluid Simulations of Upper-chromospheric Magnetic Reconnection with Helium–Hydrogen Mixture

Q. M. Wargnier^{1,2}, J. Martínez-Sykora^{1,2,3,4} , V. H. Hansteen^{1,2,3,4} , and B. De Pontieu^{1,3,4} ¹Lockheed Martin Solar & Astrophysics Laboratory, 3251 Hanover St, Palo Alto, CA 94304, USA²Bay Area Environmental Research Institute, NASA Research Park, Moffett Field, CA 94035, USA³Rosseland Centre for Solar Physics, University of Oslo, P.O. Box 1029 Blindern, NO-0315 Oslo, Norway⁴Institute of Theoretical Astrophysics, University of Oslo, P.O. Box 1029 Blindern, NO-0315 Oslo, Norway

Received 2022 November 3; revised 2023 February 10; accepted 2023 February 23; published 2023 April 7

Abstract

Our understanding of magnetic reconnection (MR) under chromospheric conditions remains limited. Recent observations have demonstrated the important role of ion–neutral interactions in the dynamics of the chromosphere. Furthermore, the comparison between the spectral profiles and synthetic observations of reconnection events suggests that current MHD approaches appear to be inconsistent with observations. First, collisions and multithermal aspects of the plasma play a role in these regions. Second, hydrogen and helium ionization effects are relevant to the energy balance of the chromosphere. This work investigates the multifluid multispecies (MFMS) effects on MR in conditions representative of the upper chromosphere using the multifluid Ebysus code. We compare an MFMS approach based on a helium–hydrogen mixture with a two-fluid MHD model based on hydrogen only. The simulations of MR are performed in a Lundquist number regime high enough to develop plasmoids and instabilities. We study the evolution of the MR and compare the two approaches including the structure of the current sheet and plasmoids, the decoupling of the particles, the evolution of the heating mechanisms, and the composition. The presence of helium species leads to more efficient heating mechanisms than the two-fluid case. This scenario, which is out of reach of the two-fluid or single-fluid models, can reach transition region temperatures starting from upper-chromospheric thermodynamic conditions, representative of a quiet Sun scenario. The different dynamics between helium and hydrogen species could lead to chemical fractionation and, under certain conditions, enrichment of helium in the strongest outflows. This could be of significance for recent observations of helium enrichment in the solar wind in switchbacks and coronal mass ejections.

Unified Astronomy Thesaurus concepts: [Solar chromosphere \(1479\)](#); [Solar magnetic reconnection \(1504\)](#)

Supporting material: animations

1. Introduction

Several plasma state transitions are found in the chromosphere. Indeed, the plasma can be partially or fully ionized, weakly or strongly magnetized, weakly or strongly collisional, all depending on the region considered (see Vernazza & Mason 1978; Martínez-Sykora et al. 2020; Ni et al. 2020). Furthermore, the solar atmosphere is a complex environment composed of many species with a large range of ionization levels. In partially ionized plasmas, charged species interact with other charged and neutral particles through collisions. Recent studies have suggested that ion–neutral interaction effects play an important role in the dynamics of the low solar atmosphere and its energy balance (see Martínez-Sykora et al. 2015; Ballester et al. 2018; Soler & Ballester 2022, and references therein). Recent observations show that many dynamic and heating events, including through episodic magnetic reconnection, occur at chromospheric and transition region heights (De Pontieu et al. 2009, 2014a; Peter et al. 2014; Hansteen et al. 2017; Guo et al. 2020).

Magnetic reconnection (MR) is a relaxation of the magnetic field’s topology created by a local change in the magnetic field connectivity as described by Parker (1955). This process is due

to relevant dissipative effects in localized regions, called current sheets, where the magnetic field lines are reconnecting. This phenomenon is continuously present in the solar chromosphere (Bharti et al. 2013; Cargill 2013; Gontikakis et al. 2013; Klimchuk 2015) as revealed by a wide range of observations, including the Interface Region Imaging Spectrograph (IRIS; De Pontieu et al. 2014b) and the Swedish 1 m Solar Telescope (SST; e.g., Peter et al. 2014; Rouppe van der Voort et al. 2017; Guo et al. 2020), which provide unique observations of the dynamic outer solar atmosphere. In particular, recent observations with the IRIS and SST (Rouppe van der Voort et al. 2017; Young 2018) of strong brightenings in Si IV emission lines, “UV bursts,” reveal evidence for the formation of plasmoids in the presence of MR events. Observations with the SST reveal the presence of blob-like features at Alfvénic speed in the Ca II K line. However, the comparison between the spectral profiles of the observed plasmoids and synthetic observations of reconnection suggests that (1) the number of plasmoids is large and (2) the observed motions within the reconnection site are much more complicated than those predicted by a classical single-fluid MHD approach (Nóbrega-Siverio et al. 2017). UV bursts may span over extended regions from the upper photosphere and the chromosphere to the transition region (TR); thus, collisional and multithermal aspects of the plasma may play a role and need to be investigated (Hansteen et al. 2019).

On the one hand, several studies try to approximate collisions and multifluid aspects of the plasma by including



Original content from this work may be used under the terms of the [Creative Commons Attribution 4.0 licence](#). Any further distribution of this work must maintain attribution to the author(s) and the title of the work, journal citation and DOI.

the generalized Ohm’s law with ambipolar diffusion (see, e.g., Leake & Arber 2006; Khomenko et al. 2018; Martínez-Sykora et al. 2020; Rempel & Przybylski 2021). This approach is generally used to simulate the solar atmosphere and accounts for ion–neutral interactions while retaining the simplicity of a single-fluid approach. On the other hand, several two-fluid MHD models (e.g., Leake & Linton 2013; Alvarez Laguna et al. 2016; Ni & Lukin 2018; Popescu Braileanu et al. 2019; Ni et al. 2020; Wójcik et al. 2020; Niedziela et al. 2021; Pelekhata et al. 2021) have been constructed to investigate the collisions and multithermal aspects of the plasma in the solar chromosphere. In that framework, the two fluids can interact through collisions and reactions, while the ions and electrons can interact with the electromagnetic field. Alternatively, the multicomponent model (e.g., Graille et al. 2009; Wargnier et al. 2018; Wargnier 2019) has been derived from kinetic theory and developed from a multiscale analysis of the nondimensional Boltzmann equations for electrons and heavy species using a generalized Chapman–Enskog expansion. Note that, to be consistent with previous work involving multicomponent plasmas (e.g., Wargnier et al. 2018; Wargnier 2019), we refer to heavy particle or heavy species any species that has a mass considered asymptotically much larger than the mass of the electrons, i.e., any species of a given plasma mixture except electrons. This model is a sound alternative to two-fluid models and is suitable for both partially and fully ionized multicomponent plasmas. Moreover, it accounts for the thermal nonequilibrium between the heavy particles (any ions and neutrals) and the electrons with a rigorous and detailed description of the dissipative effects based on kinetic theory of gases.

In Leake et al. (2012) and Leake & Linton (2013), a study of MR with a two-fluid simulation of MR for a weakly ionized reacting plasma, focusing on the solar chromosphere by considering collisions, the thermal nonequilibrium between ions and neutrals, ionization/recombination, and optically thin radiative losses was performed. The studies cited above focus on a two-fluid approach based on a single species with one ionized level of hydrogen. However, the Sun has additional species (such as helium and ionized metals) all with several excited and ionized levels with different degrees of magnetization and collisional cross sections that could potentially change the thermodynamics of the MR and its topology. Additionally, recent studies show evidence of the importance of helium ionization in the energy balance of the solar chromosphere, as shown in Hansteen et al. (1997), Golding et al. (2014, 2016, 2017), and Martínez-Sykora et al. (2020). It has been demonstrated that the helium ionization state is often far from local thermodynamic equilibrium and that models require that both the temporal state and photoionization and collisional-ionization effects are considered in order to be consistent with observations. Therefore, the most recent multifluid simulations of reconnection lack the self-consistent treatment of the relevant physical processes involved in the solar atmosphere, such as decoupling between various types of species, like hydrogen or helium species, including their respective ionized and excited levels.

In solar chromospheric conditions, and also in other astrophysical environments (Gosling 2007; Pucci et al. 2020b), MR processes mostly evolve in high-Lundquist-number regimes. In this regime, current sheets become rapidly unstable to resistive tearing instabilities, which produces

plasmoids (e.g., Bhattacharjee et al. 2009, 2010; Pucci et al. 2020b). Plasmoids are believed to play a major role in speeding up reconnection by having an influence on the variation of the current sheet size, as shown by Murtas et al. (2021). Under the formation of plasmoids, the current sheet breaks into fragments or sections (see Leake et al. 2020) and the resulting high current densities in each of these sections facilitate a high reconnection rate, as shown by Leake et al. (2012) and Leake & Linton (2013). Plasmoid formation due to the instability of Sweet–Parker current sheets has been extensively examined through numerical studies with single fluids (Steinolfson & Hoven 1984; Ugai 1995; Loureiro et al. 2005; Loureiro & Uzdensky 2015; Guo et al. 2020; Leake et al. 2020). Recent works have proved that in fully ionized plasmas it is possible to trigger plasmoids for a critical Lundquist number S_c ranging from 10^3 to 10^4 , as described by Bhattacharjee et al. (2009), Cassak et al. (2009), Huang & Bhattacharjee (2010), and Ni et al. (2010). However, many studies have also demonstrated that this critical Lundquist number may vary by several orders of magnitude depending on the initial setup, such as the current sheet configuration, the amplitudes of viscosity and perturbations, and the plasma beta coefficient β_p (see Ni et al. 2012, 2013; Huang et al. 2017). Additionally, the role of partial ionization on the onset of MR and development of the resistive tearing instability has been demonstrated (Zweibel et al. 2011; Pucci et al. 2020a; Murtas et al. 2021). However, most of these studies consider only hydrogen species and do not consider additional species such as helium. Therefore, we aim to expand the studies of plasmoid formation and instabilities by including several species.

Recent measurements from the Solar Wind Electrons Alphas and Protons (SWEAP) and FIELDS on board the Parker Solar Probe (Kasper et al. 2015) revealed that Alfvénic magnetic field reversals called switchbacks (SBs) are associated with a significant increase in alpha particle abundances at the upper layers of the solar atmosphere (Bale et al. 2021). Even though the SBs origin is not clear and could be associated with different possible mechanisms (magnetic reconnections, nano-flares, wave dissipation, footpoint shearing, or turbulence), observed SBs are characterized by strong periodic spatial modulations of the amplitude of the magnetic fields combined with a large increase in the number of alpha particles at coronal height. This spatial characteristic scale is consistent with solar supergranulation scales suggesting that the driver is connected to the supergranular network magnetic field (Bale et al. 2021; Fargette et al. 2021). These are also distinct features of a slow solar wind (Woolley et al. 2021). The chemical fractionation involving helium species should occur in the chromosphere, where plasma is partially ionized, suggesting the driver mechanism of these phenomena may be connected to this region. Addressing the chemical fractionation could help us understand the switchbacks’ drivers and slow solar wind, and may provide insight into the enhancement of alpha particles in the upper layers of the solar atmosphere.

In this work, a magnetic reconnection event in conditions typical of the upper chromosphere is studied. To do so, we consider an initial setup with a Lundquist number environment above the critical Lundquist number $S_c \approx 4 \times 10^3$ that leads to an instability regime characterized by the production of plasmoids (see Murtas et al. 2021) and references therein. The multifluid multispecies (MFMS) model accounts for multiple species with different ionized and excited levels, as

described by Martínez-Sykora et al. (2020). We aim to study many fundamental physical processes and assess their impact on the reconnection process. By focusing on one scenario of a magnetic reconnection event, we perform two simulations based on two different mixtures: a two-fluid (TF) hydrogen mixture based on H, H⁺, and electrons and an MFMS hydrogen–helium mixture based on H, H⁺, He, He⁺, and electrons. This allows highlighting the impact of helium species with different ionized levels on the reconnection process. Additionally, we assess the impact of the MFMS and two-fluid approach on the structure of plasmoids and their formation.

The structure of this paper is as follows. In Section 2, the MFMS and TF model and their assumptions are described. Section 3 briefly describes the numerical methods considered in Ebysus. The initial conditions of the MRs simulations are inspired by upper-chromospheric conditions (Section 4). In Section 5, we analyze the results of the numerical simulations based on the MFMS and TF models at different levels: the structure of the current sheet and plasmoids, the velocity fields and decoupling between species, and the evolution of the heating processes and composition of the plasma. Finally, Section 6 contains the discussion and the summary.

2. Multifluid Multispecies and Two-fluid Governing Equations

We briefly summarize the TF and MFMS MHD governing equations and their assumptions. Note that all equations are written in SI units. For the MFMS model, we focus on a hydrogen–helium mixture \mathcal{M} such that $\mathcal{M} = \mathcal{H} \cup \{\epsilon\}$, where $\mathcal{H} = \{\text{H}, \text{H}^+, \text{He}, \text{He}^+\}$ and ϵ denotes the set of heavy particles and electrons, respectively. Conversely, the TF model has a pure hydrogen mixture $\mathcal{M}_{\text{TF}} = \mathcal{H}_{\text{TF}} \cup \{\epsilon\}$, where $\mathcal{H}_{\text{TF}} = \{\text{H}, \text{H}^+\}$. No excited levels will be considered in this work. $n_{\mathcal{M}}$ and $n_{\mathcal{H}}$ denote the number of species in \mathcal{M} and \mathcal{H} , respectively.

For clarity and consistency, we use a similar nomenclature to that used by Ballester et al. (2018) and Khomenko & Collados (2014) with minor adjustments. The ionization states are referred to as \mathcal{I} ; i.e., $\mathcal{I} = 0$ denotes neutrals and $\hat{\mathcal{I}} = \mathcal{I} \geq 1$ ions. The identity of the chemical species (here hydrogen or helium) is indicated by α . Consequently, each set of particles in a given microstate is described by $\alpha\mathcal{I} \in \mathcal{M}$ or $\alpha\mathcal{I} \in \mathcal{M}_{\text{TF}}$. For electrons, the notation $\alpha\mathcal{I}$ is reduced to just $\{\epsilon\}$. In both the TF and MFMS models, we neglect the electron inertia and assume quasi-neutrality. Additionally, we neglect the viscous effects associated with electrons. Each species has its own temperature $T_{\alpha\mathcal{I}}$ and no internal degrees of freedom. Finally, we neglect the effect of gravity.

In the following, the governing equations will be written for the general case, i.e., for the MFMS model based on \mathcal{M} . The set of equations for TF based on \mathcal{M}_{TF} will be presented as a simplification of the MFMS model.

2.1. Continuity Equations for Heavy Particles

The mass density for each type of fluid in a given microstate $\alpha\mathcal{I} \in \mathcal{H}$ is governed by the continuity equation in this generic form:

$$\begin{aligned} \partial_t \rho_{\alpha\mathcal{I}} + \nabla \cdot (\rho_{\alpha\mathcal{I}} \mathbf{u}_{\alpha\mathcal{I}}) \\ = m_{\alpha\mathcal{I}} (\Gamma_{\alpha\mathcal{I}}^{\text{ion}} + \Gamma_{\alpha\mathcal{I}}^{\text{rec}}), \quad \alpha\mathcal{I} \in \mathcal{H}, \end{aligned} \quad (1)$$

where $\rho_{\alpha\mathcal{I}} = m_{\alpha\mathcal{I}} n_{\alpha\mathcal{I}}$ and $m_{\alpha\mathcal{I}}$ are the mass density and particle mass, respectively, $\mathbf{u}_{\alpha\mathcal{I}}$ is the velocity, $\Gamma_{\alpha\mathcal{I}}^{\text{rec}}$ and $\Gamma_{\alpha\mathcal{I}}^{\text{ion}}$ are the mass transition rate due to recombination or de-excitation and ionization or excitation, respectively. For any $\alpha\mathcal{I} \in \mathcal{H}$, these rates are defined as

$$\Gamma_{\alpha\mathcal{I}}^{\text{ion}} = \sum_{\alpha\mathcal{I}' \in \mathcal{H} \neq \alpha\mathcal{I}} \begin{cases} n_{\alpha\mathcal{I}'} \nu_{\alpha\mathcal{I}\mathcal{I}'}^{\text{ion}}, & \text{if } \mathcal{I} > \mathcal{I}' \\ -n_{\alpha\mathcal{I}} \nu_{\alpha\mathcal{I}\mathcal{I}'}^{\text{ion}}, & \text{otherwise,} \end{cases} \quad (2)$$

and

$$\Gamma_{\alpha\mathcal{I}}^{\text{rec}} = \sum_{\alpha\mathcal{I}' \in \mathcal{H} \neq \alpha\mathcal{I}} \begin{cases} -n_{\alpha\mathcal{I}'} \nu_{\alpha\mathcal{I}\mathcal{I}'}^{\text{rec}}, & \text{if } \mathcal{I} > \mathcal{I}' \\ n_{\alpha\mathcal{I}} \nu_{\alpha\mathcal{I}\mathcal{I}'}^{\text{rec}}, & \text{otherwise,} \end{cases} \quad (3)$$

where $\nu_{\alpha\mathcal{I}\mathcal{I}'}^{\text{ion}}$ and $\nu_{\alpha\mathcal{I}\mathcal{I}'}^{\text{rec}}$ are the ionization and recombination frequencies, respectively, between particles with microstate $\alpha\mathcal{I}$ and $\alpha\mathcal{I}' \in \mathcal{H}$. In both the MFMS and TF models, the frequencies associated with the transition rates ν^{rec} and ν^{ion} include radiative and dielectronic recombination where the rates have been taken from Aldrovandi & Pequignot (1973). The ionization and three-body recombination rates have been taken from Janev et al. (1989). Photoionization is roughly modeled by simply assuming constant rates taken from Vernazza et al. (1981) for the H–H⁺ and He–He⁺ transitions. Note that for the TF model the continuity equations presented in Equation (1) are identical to those of the MFMS model by simply changing the set of heavy particles \mathcal{H} by \mathcal{H}_{TF} .

2.2. Momentum Equations for Heavy Particles

In the MFMS model, the momentum equation associated for a given species defined by its microstate $\alpha\mathcal{I} \in \mathcal{H}$ is defined as follows:

$$\begin{aligned} \partial_t (\rho_{\alpha\mathcal{I}} \mathbf{u}_{\alpha\mathcal{I}}) + \nabla \cdot (\rho_{\alpha\mathcal{I}} \mathbf{u}_{\alpha\mathcal{I}} \otimes \mathbf{u}_{\alpha\mathcal{I}} + P_{\alpha\mathcal{I}} \mathbb{I} - \boldsymbol{\tau}_{\alpha\mathcal{I}}) \\ = n_{\alpha\mathcal{I}} q_{\alpha\mathcal{I}} (\mathbf{E} + \mathbf{u}_{\alpha\mathcal{I}} \wedge \mathbf{B}) \\ + \mathbf{R}_{\alpha\mathcal{I}}^{\text{ion}} + \mathbf{R}_{\alpha\mathcal{I}}^{\text{rec}} + \mathbf{R}_{\alpha\mathcal{I}}^{\text{col}}, \quad \alpha\mathcal{I} \in \mathcal{H}, \end{aligned} \quad (4)$$

where $q_{\alpha\mathcal{I}}$ and $P_{\alpha\mathcal{I}}$ are the ion charge and gas pressure of a given species $\alpha\mathcal{I} \in \mathcal{H}$, respectively, $\boldsymbol{\tau}_{\alpha\mathcal{I}}$ is the viscous stress tensor associated with species $\alpha\mathcal{I} \in \mathcal{H}$, \mathbf{E} and \mathbf{B} are the electric and magnetic fields, respectively, $\mathbf{R}_{\alpha\mathcal{I}}^{\text{ion}}$ and $\mathbf{R}_{\alpha\mathcal{I}}^{\text{rec}}$ are the changes in momentum for species $\alpha\mathcal{I}$ due to ionization and recombination processes respectively, $\mathbf{R}_{\alpha\mathcal{I}}^{\text{col}}$ is the sum of all the momentum exchange between particles with a given microstate $\alpha\mathcal{I} \in \mathcal{H}$ with any other particles with another microstate $\alpha'\mathcal{I}' \in \mathcal{M}$.

In the TF model, the momentum equation given as Equation (4) slightly differs. We solve for (1) a momentum equation for neutrals (here H) and (2) a momentum equation for all ionized species that is the sum of the momentum equations for ions (here H⁺) and electrons. Therefore, the Lorentz force, corresponding to the first right-hand side term of Equation (4), reads $\mathbf{J} \wedge \mathbf{B}$, where \mathbf{J} is the total current density. Additionally, in the momentum equations for ions, the pressure term in the convective fluxes is simply replaced by the total pressure of

charged particles $\nabla \cdot ([P_{\text{H}^+} + P_e]\mathbb{I})$. Note that in the MFMS model the term associated with the gradient of the pressure of the electrons is involved in the definition of \mathbf{E} . Additionally if the coupling between ions is strong enough, then the Lorentz force for the MFMS model goes back to the classical definition ($\mathbf{J} \times \mathbf{B}$) consistently with the TF case.

In this study, we consider plasmas evolving in chromospheric conditions, that is, in high-Reynolds-number regimes. Therefore, the viscous terms are modeled numerically with hyperdiffusive terms. In this context, an artificial subgrid-scale model of these viscous terms $\tau_{\alpha\mathcal{I}}$, $\alpha\mathcal{I} \in \mathcal{M}$, or \mathcal{M}_{TF} has been considered in order to represent shocks and turbulence. This approach is inspired from Nordlund (1982) and Gudiksen et al. (2011) and has been extended for the MFMS and TF models.

In the MFMS model, the sum of all the momentum exchange for a fluid of a specific particle with a given microstate $\alpha\mathcal{I} \in \mathcal{H}$ is defined as:

$$\begin{aligned} \mathbf{R}_{\alpha\mathcal{I}}^{\text{col}} &= \sum_{\alpha'\mathcal{I}' \in \mathcal{M}} \mathbf{R}_{\alpha\mathcal{I},\alpha'\mathcal{I}'}^{\text{col}} \\ &= \sum_{\alpha'\mathcal{I}' \in \mathcal{M}} m_{\alpha\mathcal{I}} n_{\alpha\mathcal{I}} \nu_{\alpha\mathcal{I},\alpha'\mathcal{I}'}^{\text{col}} (\mathbf{u}_{\alpha'\mathcal{I}'} - \mathbf{u}_{\alpha\mathcal{I}}), \end{aligned} \quad (5)$$

where $\nu_{\alpha\mathcal{I},\alpha'\mathcal{I}'}^{\text{col}}$ is the collision frequency between particles $\alpha\mathcal{I}$ and $\alpha'\mathcal{I}'$. The momentum exchange operators are symmetric, i.e., $\forall(\alpha\mathcal{I}, \alpha'\mathcal{I}') \in \mathcal{H} \times \mathcal{M}$, $\mathbf{R}_{\alpha\mathcal{I},\alpha'\mathcal{I}'}^{\text{col}} = -\mathbf{R}_{\alpha'\mathcal{I}',\alpha\mathcal{I}}^{\text{col}}$. Note that Equation (5) does not include the term associated with the difference in heat fluxes between species, as described by Hansteen et al. (1997) or in the 13N moment model of Zhdanov (2002). The collision frequencies $\nu_{\alpha\mathcal{I},\alpha'\mathcal{I}'}^{\text{col}}$ are described in detail in Wargnier et al. (2022). In this context, the collisional frequencies are consistent with the definition given by Zhdanov (2002) in the context of the 13-N moment model for multicomponent plasmas, calculated from generalized Chapman–Cowling collision integrals. The collision integral data for \mathcal{M} and \mathcal{M}_{TF} have been taken from Bruno et al. (2010) based on a review of experimental measurements. These collision integrals include charge-exchange interactions for H–H⁺ and He–He⁺ interactions.

2.3. Thermal Energy Equations

In the MFMS and TF models, we account for thermal decoupling between all particles, including electrons. Therefore, we solve for the equations of the thermal energy for each particle $\alpha\mathcal{I} \in \mathcal{M}$ or \mathcal{M}_{TF} .

In the MFMS model, the energy equations for each heavy particle and the electrons read as follows,

$$\begin{aligned} \partial_t e_{\alpha\mathcal{I}} + \nabla \cdot (e_{\alpha\mathcal{I}} \mathbf{u}_{\alpha\mathcal{I}}) + P_{\alpha\mathcal{I}} \nabla \cdot \mathbf{u}_{\alpha\mathcal{I}} \\ = Q_{\alpha\mathcal{I}}^{\text{ion}} + Q_{\alpha\mathcal{I}}^{\text{rec}} + Q_{\alpha\mathcal{I}}^{\text{col}} + Q_{\alpha\mathcal{I}}^{\tau}, \quad \alpha\mathcal{I} \in \mathcal{H}, \end{aligned} \quad (6)$$

$$\begin{aligned} \partial_t e_e + \nabla \cdot (e_e \mathbf{u}_e) + P_e \nabla \cdot \mathbf{u}_e \\ = Q_e^{\text{ion}} + Q_e^{\text{rec}} + Q_e^{\text{col}} + Q_e^{\text{spitz}}, \end{aligned} \quad (7)$$

where $e_{\alpha\mathcal{I}}$ and e_e are the thermal energies of any heavy particle $\alpha\mathcal{I} \in \mathcal{H}$ and the electrons, respectively. $Q_{\alpha\mathcal{I}}^{\text{ion}} + Q_{\alpha\mathcal{I}}^{\text{rec}}$ and

$Q_e^{\text{ion}} + Q_e^{\text{rec}}$ are the heating/cooling terms due to the ionization and recombination processes associated with particles $\alpha\mathcal{I} \in \mathcal{H}$ and electrons, respectively, Q_e^{spitz} is the heating term due to the electron thermal conduction along the magnetic field, $Q_{\alpha\mathcal{I}}^{\tau}$ is the heating term due to viscous effects associated with particle $\alpha\mathcal{I} \in \mathcal{H}$, $Q_{\alpha\mathcal{I}}^{\text{col}}$ and Q_e^{col} are the heating terms due to collisions associated with heavy particle $\alpha\mathcal{I} \in \mathcal{H}$ and electrons, respectively. In the TF model, the energy equations Equations (6) and (7) are obtained by substituting $\alpha\mathcal{I} \in \mathcal{H}_{\text{TF}}$ to $\alpha\mathcal{I} \in \mathcal{H}$.

Note that Q_e^{ion} corresponds to the optically thin radiative losses term, which involve the hydrogen and helium ionization potential coefficients, as described by Leake et al. (2012) and Leake & Linton (2013). The Spitzer term is anisotropic with respect to the magnetic field and is identical to the definition from Spitzer (1956) and Gudiksen et al. (2011). The heating term due to viscous effects $Q_{\alpha\mathcal{I}}^{\tau}$ is derived from the viscous terms in the momentum equations $\tau_{\alpha\mathcal{I}}$ leading to a similar expression introduced by Nordlund (1982) and Gudiksen et al. (2011) for a single-fluid MHD model.

The collisional terms associated with any particle $\alpha\mathcal{I} \in \mathcal{M}$ are defined as

$$Q_{\alpha\mathcal{I}}^{\text{col}} = \sum_{\alpha'\mathcal{I}' \in \mathcal{M}} Q_{\alpha\mathcal{I},\alpha'\mathcal{I}'}^{\text{col}} = \sum_{\alpha'\mathcal{I}' \in \mathcal{M}} Q_{\alpha\mathcal{I},\alpha'\mathcal{I}'}^{u,\text{col}} + Q_{\alpha\mathcal{I},\alpha'\mathcal{I}'}^{T,\text{col}}. \quad (8)$$

The first component of Equation (8) corresponds to the heating produced by the drift velocity between species $(\alpha\mathcal{I}, \alpha'\mathcal{I}') \in \mathcal{M}^2$ due to collisions. The second component corresponds to a thermalization process where the temperature $T_{\alpha\mathcal{I}}$ relaxes toward $T_{\alpha'\mathcal{I}'}$ at a collisional rate $\nu_{\alpha\mathcal{I},\alpha'\mathcal{I}'}^{\text{col}}$. The heating produced by the drift velocity and thermalization terms between species $\alpha\mathcal{I}$ and $\alpha'\mathcal{I}'$ are defined as

$$\begin{aligned} Q_{\alpha\mathcal{I},\alpha'\mathcal{I}'}^{u,\text{col}} &= \nu_{\alpha\mathcal{I},\alpha'\mathcal{I}'}^{\text{col}} m_{\alpha\mathcal{I},\alpha'\mathcal{I}'} n_{\alpha\mathcal{I}} |\mathbf{u}_{\alpha'\mathcal{I}'} - \mathbf{u}_{\alpha\mathcal{I}}|^2, \\ Q_{\alpha\mathcal{I},\alpha'\mathcal{I}'}^{T,\text{col}} &= \nu_{\alpha\mathcal{I},\alpha'\mathcal{I}'}^{\text{col}} \left(\frac{3m_{\alpha\mathcal{I}}}{m_{\alpha\mathcal{I}} + m_{\alpha'\mathcal{I}'}} \right) n_{\alpha\mathcal{I}} k_B (T_{\alpha'\mathcal{I}'} - T_{\alpha\mathcal{I}}). \end{aligned} \quad (9)$$

Note that for any $(\alpha\mathcal{I}, \alpha'\mathcal{I}') \in \mathcal{M}^2$ or $\mathcal{M}_{\text{TF}}^2$, the thermalization terms $Q_{\alpha\mathcal{I},\alpha'\mathcal{I}'}^{T,\text{col}}$ do not contribute to the total thermal energy (sum of all the thermal energy equations Equations (6) and (7)) of the multifluid plasma as these terms are symmetric with respect to species. Similarly, for any $\alpha\mathcal{I} \in \mathcal{H}$ or \mathcal{H}_{TF} , the ionization/recombination terms of heavy species $Q_{\alpha\mathcal{I}}^{\text{ion}} + Q_{\alpha\mathcal{I}}^{\text{rec}}$ do not contribute to the total thermal energy. However, the heating produced by drift velocities, optically thin radiative losses, and Spitzer terms contribute to the total thermal energy.

2.3.1. Equation of States

In both the MFMS and TF models, we assume equation of states for electrons and heavy species following classical ideal gases laws such as

$$P_{\alpha\mathcal{I}} = n_{\alpha\mathcal{I}} k_B T_{\alpha\mathcal{I}} = (\gamma - 1) e_{\alpha\mathcal{I}}, \quad \alpha\mathcal{I} \in \mathcal{H} \text{ or } \mathcal{H}_{\text{TF}} \quad (10)$$

and

$$P_e = n_e k_B T_e = (\gamma - 1) e_e, \quad (11)$$

where $\gamma = 5/3$ is the adiabatic constant taken as identical for all species.

2.4. Generalized Ohm's Law and Magnetic Induction Equation

In both the MFMS and TF models, we compute the electric field from a simplified electron momentum equation in the asymptotic limit where we assume that (1) the electron inertia and its time variation is neglected, (2) the mass of electrons is much smaller than the mass of any heavy particles, and (3) the effects associated with ionization and recombination are neglected. In this framework, in both the MFMS and TF models, Ohm's law reads

$$\mathbf{E} = -\mathbf{u}_e \wedge \mathbf{B} + \frac{1}{n_e q_e} [\nabla P_e - \mathbf{R}_e^{\text{col}}], \quad (12)$$

where $\mathbf{R}_e^{\text{col}}$ has the same definition as Equation (5) by replacing a given heavy species $\alpha\mathcal{I} \in \mathcal{H}$ by $\alpha\mathcal{I} = \{e\}$. The electromagnetic field is not considered as an external force but their evolution is governed by the set of Maxwell equations. Therefore, by combining Equation (12) with the Maxwell–Faraday equation,

$$\partial_t \mathbf{B} = -\nabla \wedge \mathbf{E}, \quad (13)$$

we obtain the magnetic induction equation.

In the MFMS model, as several ionized species are considered and the quasi-neutrality approximation is assumed, the electron velocity can be expressed as a function of the hydrodynamic velocity of each ion and the total current as follows

$$\mathbf{u}_e = \sum_{\alpha\mathcal{I}} \frac{n_{\alpha\mathcal{I}} q_{\alpha\mathcal{I}} \mathbf{u}_{\alpha\mathcal{I}}}{n_e q_e} - \frac{\mathbf{J}}{n_e q_e}. \quad (14)$$

Note that the contribution of the total current \mathbf{J} of the electron velocity in the equation of the electric field in Equation (12), also known as the Hall term, has not been considered for this study (however, we will investigate the effect of this term in future studies). Indeed, in this work, as a first step, we began by examining a simplified version of the MFMS and TF models, in particular analyzing the interactions between species, collisions, ionization, and recombination processes. Future research will include more advanced and realistic models that incorporate the Hall term.

In this study, as the characteristic speed of each particle is much smaller than the speed of light in vacuum, the Maxwell–Ampere's law can be simplified by neglecting the displacement current term, which leads to the following relation of the total current

$$\mathbf{J} = (\nabla \wedge \mathbf{B}) / \mu_0, \quad (15)$$

where μ_0 is the vacuum permeability. In this context, drift waves are not taken into account (Vranjes & Poedts 2009). Note that from Equation (12) it is possible to identify one component of the resistivity of the MFMS model as function of the collision integrals; see Appendix A for further details.

The set of equations associated with the MFMS and TF models described in Equations (1), (4), (6), (7), and (13) is a closed system of equations, which can be solved and integrated with a specific numerical strategy. As $n_{\mathcal{H}} = 4$ and $n_{\mathcal{H}_{\text{TF}}} = 2, 24$

and 14 equations have to be solved in the MFMS and TF models, respectively.

3. Numerical Methods

The two sets of governing equations for the MFMS and TF models presented in Equations (1), (4), (6), (7), and (13) have been implemented in a code named Ebysus (Martínez-Sykora et al. 2020), which is an extension of the single-fluid radiative MHD code Bifrost (Gudiksen et al. 2011). Note that the governing equations can be rewritten in a more compact form, which allows us to distinguish the nature of the different terms involved, as shown in Appendix B.

Concerning the spatial discretization, a sixth-order differential operator has been considered for the convective fluxes, as in Bifrost. The conservative quantities are not co-located in space and are considered on a staggered grid; thus, a fifth-order interpolation is used to relocate variables as needed. As a high-order finite-difference scheme has been considered, it is convenient to numerically stabilize shocks and discontinuities with artificial numerical terms. In the literature, several type of artificial terms have been introduced, as described by Wilkins (1980), Cook & Cabot (2005), and references therein. By inheritance of the Bifrost code, the structure of the artificial terms are the hyperdiffusive terms described by Nordlund (1982) and Gudiksen et al. (2011). These terms are considered in order to capture shocks and discontinuities while treating correctly turbulence in a high-Reynolds-number regime. In Ebysus the hyperdiffusive terms have been expanded for the multifluid case from those considered in Bifrost as they depend on the velocity and speed of sound for each species and the Alfvén speed of all ions. The constant coefficients introduced in these terms have been chosen based on fits to a wide variety of shock and turbulence test problems.

The integration of the two presented systems requires some specific temporal integration methods. Indeed, these systems can be seen as convective–diffusive systems with stiff source terms (see Descombes & Massot 2004; Abdulle & Vilmart 2013; Duarte et al. 2013), as presented in Appendix B. Some of these source terms (in particular those associated with collisions and ionization/recombination) are numerically stiff as they are associated with physical processes where timescales are often much smaller than the convective timescales. Therefore, these terms are subject to strong Courant–Friedrichs–Lewy constraints leading to small time steps and drastically increased computational costs. To avoid this, our strategy is to consider a first-order Lie splitting approach in order to split the temporal integration into different subsystems. First, the convective terms have been integrated following a third-order predictor–corrector Hyman (Hyman et al. 1979). Alternatively, it is possible to consider a third-order explicit Runge–Kutta method. Then, the diffusive term (i.e., the Spitzer term) has been integrated by solving a non-Fickian (hyperbolic) diffusion equation as described by (see Rempel 2016). Note that, in Ebysus, it is possible to integrate this term following an implicit multigrid method, as described in Gudiksen et al. (2011). Finally, the stiff source terms (see S^{stiff} in Appendix B) are integrated following an ordinary differential equation solver based on a fifth-order implicit Runge–Kutta method also known as *Radau IIA* method (see Hairer & Wanner 1996, 1999). In order to maintain the solenoidal constraint on the magnetic field, a Hodge projection method has been used (see Brackbill & Barnes 1980). We have implemented a numerical strategy to

minimize computational expenses while ensuring that the simulation for a 2.5D case does not exceed one week. The resulting computational times for the MFMS and TF models are 150 and 48 hr, respectively.

Ebysus allows the introduction of as many species as desired using DIPER format atom files and the CHIANTI database (see Judge 2007; Del Zanna et al. 2015). The number of ionized and excited levels, transitions, and rates are detailed in these atom files. The code allows one to easily perform numerical simulations with any chosen mixtures following identical numerical strategies focusing on the system of equations presented in the previous section, as long as the atom files associated with all species considered are provided. The Ebysus code also has the possibility of running a single-fluid MHD option allowing a comparison with multifluid MHD models using the same numerical code.

4. Methodology and Initial Conditions

In this study, we focus on a magnetic reconnection configuration under specific thermodynamic conditions that aim to represent the upper solar chromosphere. For identical initial thermodynamic conditions, we perform a comparison between the TF model based on \mathcal{M}_{TF} (similar to what was performed by Leake et al. 2012; Leake & Linton 2013; Alvarez Laguna et al. 2016) and the MFMS model based on \mathcal{M} . Our comparison highlights the impact of helium on the reconnection process.

4.1. Initial Reconnection Setup

The reconnection setup is inspired from Leake et al. (2012) and Leake & Linton (2013), i.e., a magnetic field configuration forming a Harris current sheet placed in a constant thermodynamic and plasma beta environment. In this work, we consider an initial temperature of $T_0 = 16,000$ K and a total number density $n_0 = 7.47 \times 10^9 \text{ cm}^{-3}$. Then, the population associated with each species involved in \mathcal{M} and \mathcal{M}_{TF} is calculated. By doing so, all the total conservative quantities such as the total number density, pressure, temperature, and energy are identical at the initial conditions between the two models.

In both the MFMS and TF models, the plasma beta coefficient is calculated from the total pressure of the plasma $P_0 = n_0 k_B T_0$ and is defined as $\beta_p = 0.2$. We have considered a 2.5D domain based on a uniform grid, with 800×800 grid points, where each grid cell size is $dy = dz = 5.333$ km. In this configuration, the entire computational domain represents a 2.5D box of size $L_0 = 4.2664$ Mm. Open boundary conditions have been considered in all directions for all the variables and fields with linear extrapolations while minimizing strong gradients. In order to mitigate reflections, the last 0.1332 Mm grid points inside the domain are dedicated for extrapolating the fields and damping waves that could eventually disturb the reconnection site.

The Harris current sheet, as described by Leake et al. (2012) and Leake & Linton (2013), is defined as follows

$$\mathbf{A}_x = -\frac{B_0}{2} \lambda_\psi \log \left(\cosh \left(\frac{y}{\lambda_\psi} \right) \right) \mathbf{e}_x, \quad \mathbf{B} = [\nabla \wedge \mathbf{A}_x], \quad (16)$$

where λ_ψ is the initial thickness of the current sheet defined as $\lambda_\psi = 0.1L_0$, B_0 is the amplitude of the magnetic field (in

Table 1
Initial Number and Mass Densities in Percentage for the MFMS and TF Models

	H		H ⁺		He	He ⁺
	\mathcal{M}	\mathcal{M}_{TF}	\mathcal{M}	\mathcal{M}_{TF}		
n [%]	34.55	37.5	57.55	62.5	7.9	3.17×10^{-6}
ρ [%]	28	37.5	46.6	62.5	25.4	10^{-5}

Note. The initial number and mass densities in percentage are calculated as $\alpha_{\alpha\mathcal{X}} [\%] = 100 \times \alpha_{\alpha\mathcal{X}} / \sum_{\alpha\mathcal{X} \in \beta} \alpha_{\alpha\mathcal{X}}$, $\alpha \in \{n, \rho\}$ and $\beta \in \{\mathcal{H}, \mathcal{H}_{\text{TF}}\}$.

balance with the total pressure $P_0 = \beta_p \frac{B_0^2}{2\mu_0}$ equal to 1.42 G, \mathbf{A}_x is the initial magnetic potential in the x direction, and \mathbf{e}_x is the elementary vector in the x direction.

The pressure of the ionized species P^{ions} is locally increased in the current sheet in order to balance the decrease in the Lorentz force in the current sheet, as follows:

$$P^{\text{ions}}(y) = P_0^{\text{ions}} + \frac{P_0^{\text{ions}}}{\cosh^2 \left(\frac{y}{\lambda_\psi} \right)}, \quad (17)$$

where P_0^{ions} is the total pressure of the ions computed from the initial thermodynamic conditions (T_0 and ρ_0). In order to trigger the reconnection we have considered a local-centered perturbation on the magnetic field (while guaranteeing the divergence free of the magnetic field) as follows:

$$\mathbf{B}_z^\alpha(y, z^*) = -\alpha \left(y - \frac{L_0}{2} \right) f(y, z^*) \mathbf{e}_z, \quad (y, z^*) \in [0, L_0]^2, \quad (18)$$

$$\mathbf{B}_y^\alpha(y, z^*) = \alpha \left(z^* - \frac{L_0}{2} \right) f(y, z^*) \mathbf{e}_y, \quad (y, z^*) \in [0, L_0]^2, \quad (19)$$

where

$$f(y, z^*) = \exp \left(- \left[\frac{z^* - L_0/2}{\lambda_\psi} \right]^2 \right) \exp \left(- \left[\frac{y - L_0/2}{\lambda_\psi} \right]^2 \right), \quad (20)$$

where α is the amplitude of the perturbation, which has been chosen in such a way that the maximum amplitude of $|\mathbf{B}^\alpha| = \sqrt{|\mathbf{B}_y^\alpha|^2 + |\mathbf{B}_z^\alpha|^2}$ corresponds to approximately 10% of the amplitude of the magnetic field of the Harris current sheet B_0 . This amplitude is chosen in accordance with Alvarez Laguna et al. (2016) and Leake et al. (2012).

For both the MFMS and TF models, the characteristic initial Alfvén speed is calculated as $V_0^{\text{Alf}} = B_0 / \sqrt{\mu_0 \rho_0^{\text{ions}}} = 60 \text{ km s}^{-1}$, where ρ_0^{ions} is the total initial mass density of ions. The initial thermal speed is $V_0^{\text{therm}} = \sqrt{8k_B T_0 / \pi m_0} = 18.3 \text{ km s}^{-1}$, where m_0 is the characteristic mass chosen here as the mass of

Table 2Initial Range of Values (Minimum/Maximum) in Statistical Equilibrium of Collision Frequencies in s^{-1} and Mean Free Path in km for the MFMS Model in Orders of Magnitude

	H-H ⁺	H-He	H ⁺ -He	He ⁺ -H	He ⁺ -H ⁺	He ⁺ -He	e-H	e-He
$\nu^{\text{col}} (\text{s}^{-1})$	$\approx 10\text{--}100$	$\approx 0.1\text{--}1$	$\approx 0.1\text{--}1$	$\approx 0.1\text{--}1$	$\approx 100\text{--}1000$	$\approx 1\text{--}5$	$100\text{--}500$	$\approx 20\text{--}50$
$\lambda_p (\text{km})$	$\approx 0.1\text{--}1$	$\approx 10\text{--}100$	$\approx 10\text{--}100$	$\approx 10\text{--}100$	$\approx 0.01\text{--}0.1$	$\approx 3\text{--}7$	$\approx 2\text{--}3$	$\approx 15\text{--}30$

Note. All other interactions not shown in this table (for example e-H⁺) have a mean free path largely below 0.01 km.

protons. No initial velocity field is considered, rather the velocity field is naturally triggered during the reconnection process. The numerical simulations based on the MFMS and TF models have been run until $t_{\text{end}} = 454$ s and 325 s, respectively. For the rest of this work, we will focus on a restricted domain in the z direction where $z \in [0, 4]$ Mm and considering the change of variable $z = z^* - \delta_z$ with $\delta_z = 0.1332$ Mm.

4.2. Initial Composition

In both the TF and MFMS models, the initial number and mass densities for all species are calculated from the total number density n_0 and temperature T_0 assuming statistical and thermal equilibrium. The initial total number density of the plasma is the same for the MFMS and TF models but the total mass density differs due to the presence of neutral helium species in the MFMS model. The initial composition of the number and mass densities for mixtures \mathcal{M} and \mathcal{M}_{TF} is given in Table 1. Note that, in the MFMS model, the initial abundance of the helium species, i.e., with respect to the total hydrogen number density, is approximately 8.5%, i.e., photospheric abundances (Asplund et al. 2009).

4.3. Initial Multifluid Parameters

In our initial setup, the rates associated with ionization or recombination processes have orders of magnitude ranging from 10^{-4} to $10^{-1.5} \text{ s}^{-1}$ for helium and hydrogen, respectively. For the MFMS model, the initial values of the collisional frequencies and mean free paths (taken as the thermal speed of the colliding species times collisional frequencies between the two species) of the different interactions in orders of magnitude are presented in Table 2. These values highlight the large disparities in the coupling between fluids due to collisions in the MFMS model. We consider plasmas evolving in chromospheric conditions, i.e., in high-Reynolds-number regimes. Therefore, the viscous terms are modeled numerically with hyperdiffusive terms. Note that in the TF model, the collisional rate between H and H⁺ is slightly higher than in Table 2 for the MFMS model due to the initial mass density of H⁺, which is higher in the TF model than in the MFMS model, as shown in Table 1.

These preliminary calculations demonstrate that the different fluids involved in the MFMS model are expected to be strongly or weakly coupled due to collisions at the initial stage of the reconnection. For example, interactions involving He-He⁺ appear to be less coupled due to collisions than interaction H-H⁺ by 2 orders of magnitude. However, interactions associated with He⁺ and H⁺ are more strongly coupled due to collisions than the H-H⁺ interaction. Note that timescales associated with ionization and recombination are much slower than the collisional timescales; thus, collisional processes are much faster than ionization and recombination processes.

As described previously, the density and temperature of each species will evolve during the reconnection process. In this context, most mean free paths (in particular those associated with H-H⁺, He-H⁺, He-He⁺, or He⁺-H⁺) will change and increase over time and, thus, are spatially resolved by the chosen grid size in those regions of interest. It is important to note that, if the mean free path of any two pairs of species is significantly smaller than the grid size at any time, these species can be considered to have a strong coupling, and thus, exhibit behavior akin to that of a single fluid.

Due to computational expenses, some of the mean free paths are not spatially resolved by the grid size, in particular those associated with Coulomb interactions (except He⁺-H⁺ interactions) or those involving electrons. Therefore, the decoupling of these interactions is not fully resolved by the current numerical setup and requires a higher spatial resolution. However, preliminary calculations with higher spatial resolutions have shown that the decoupling between helium and hydrogen species mainly dominates the evolution of the reconnection. Therefore, the chosen grid size is sufficient to resolve the coupling and decoupling of the hydrogen and helium species. Therefore, for our understanding, it is not necessary to have a higher spatial resolution and capture the decoupling between electrons and heavy particles or charged species (except He⁺-H⁺ interactions).

5. Results

In this section, we analyze the results of our two simulations based on the MFMS and TF models, keeping in mind that the mixture associated with the MFMS model is $\mathcal{M} = \{\text{H}, \text{H}^+, \text{He}, \text{He}^+, \text{e}\}$, and the mixture associated with the TF model is $\mathcal{M}_{\text{TF}} = \{\text{H}, \text{H}^+, \text{e}\}$. The analysis is performed at different levels. First, we focus on the structure of the current sheet and its evolution (Section 5.1) and then the velocity fields, and highlight the decoupling between fluids (Section 5.2). We continue with Section 5.3 in which we identify the main heating processes in both mixtures. Finally, we analyze the evolution of the ionization level in the current sheet in the MFMS and TF models and the chemical fractionation between the helium and hydrogen species in the MFMS model during the reconnection process (Section 5.4).

5.1. Current Sheet and Plasmoids

In both the MFMS and TF models, our calculations show that two phases of the reconnection process can be identified. Figure 1 and the associated animation illustrate the distribution of the orthogonal current \mathbf{J}_x and total velocity fields in both the y and z directions for both the MFMS and TF models, at different times. The total velocity fields are calculated as $\mathbf{u}_{\text{tot}} = (\rho\mathbf{u})_{\text{tot}}/\rho_{\text{tot}}$. Note that further details about each individual velocity are given in Section 5.2.

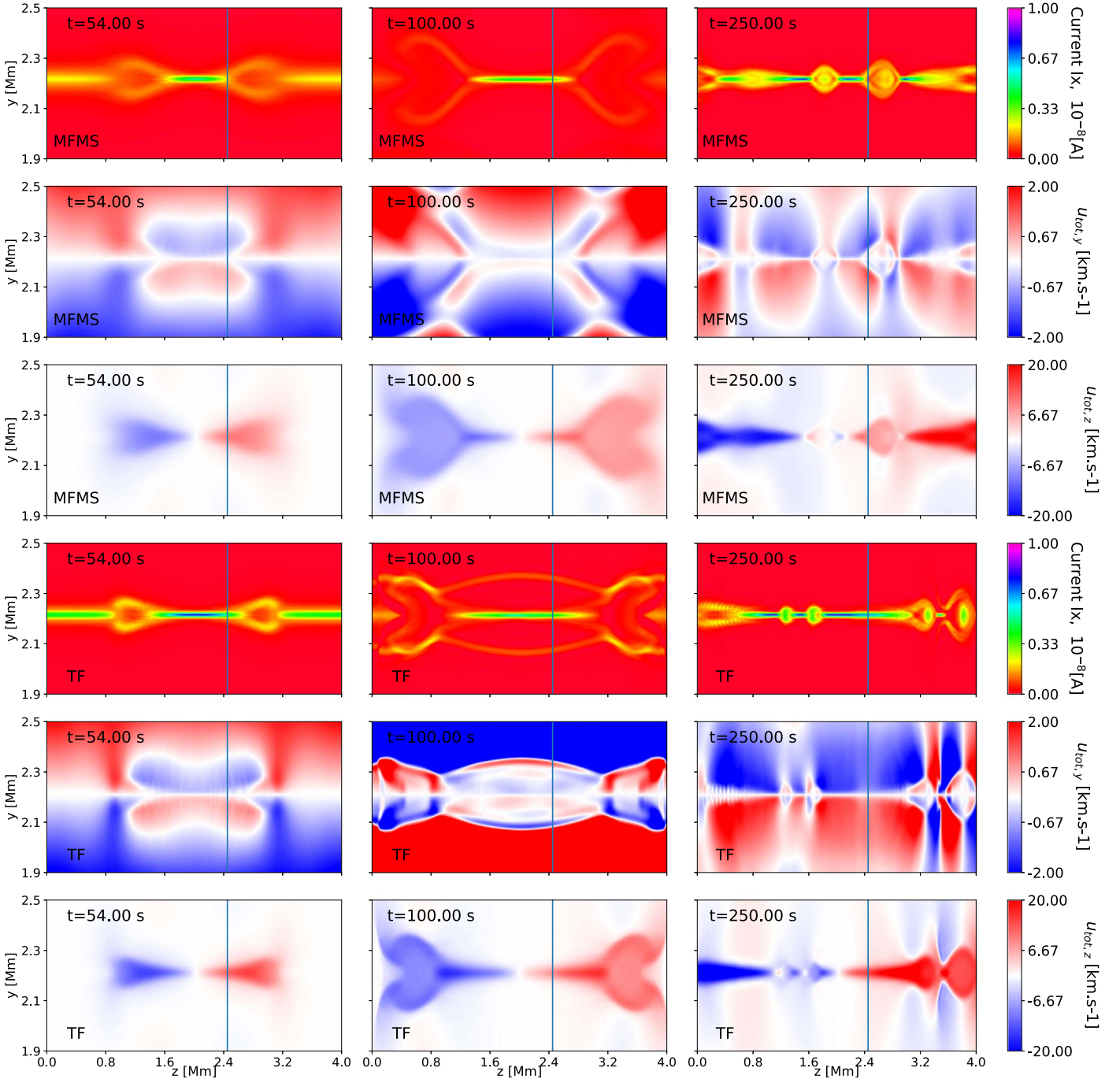


Figure 1. Distribution of component x of the current density J_x in Ampère and total velocity in km s^{-1} in the y and z directions corresponding to the inflow and outflow directions of the reconnection region, respectively, for the MFMS case (first three rows) and TF case (last three rows) in a restricted domain defined as $(y, z) \in [1.9, 2.5] \times [0, 4]$ Mm. From left to right: evolution of these distributions at $t = 54, 100,$ and 250 s. The vertical line corresponds to $z = 2.45$ Mm. The associated animation of this figure shows the time evolution from 0.50 to 327.50 s. The real-time duration of the animation is 33 s.

(An animation of this figure is available.)

First, the simulation has a laminar or a Sweet–Parker reconnection phase, where only one elongated current sheet is formed and develops inflow and outflow velocity fields corresponding to the y and z directions, respectively (see Parker 1955, 1963; Sweet 1958) due to the initial structure of the magnetic field. This can be clearly identified for both the MFMS and TF models in the first column of Figure 1, as well as in the animation corresponding to this figure. After this first phase, we have a plasmoid instability phase where many plasmoids are formed and are advected from the middle of the

reconnection region toward the outflow region along the z -axis (the last column of Figure 1). During this phase, the presence of plasmoids breaks the current sheet into multiple thinner current sheets, which reconnect faster than in the Sweet–Parker regime (see Murtas et al. 2021). This is also in agreement with previous 2D (e.g., Huang & Bhattacharjee 2010) and 3D (e.g., Huang & Bhattacharjee 2016) simulations.

At the very beginning of the laminar phase ($t \approx 54$ s), the magnitude of the current inside the reconnection region is slightly higher in the TF model than in the MFMS model, as

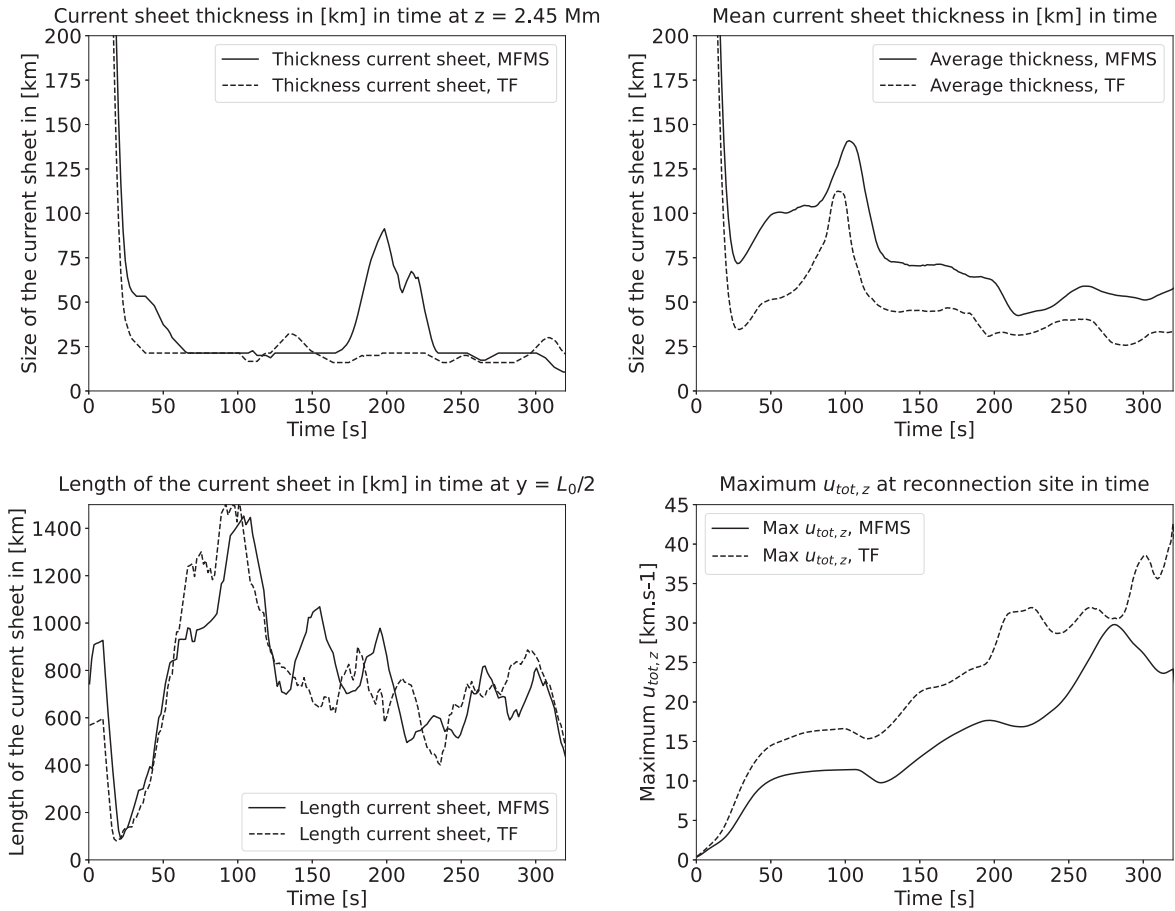


Figure 2. Evolution in time of the thickness at a fixed $z = 2.45$ Mm (top left), mean thickness for $y \in [1, 3.5]$ Mm (top right) and length of the current sheet (bottom left), and maximum total velocity in the z direction estimated at the outflow of the main reconnection site (bottom right), by taking the FWHM of the maximum current density J_x . The dashed and solid lines correspond to the TF and MFMS models, respectively. Note that $z = 2.45$ Mm is illustrated in Figure 1 by the black vertical line.

shown in the animation of Figure 1. Additionally, the magnitude of the total velocity fields close to the current sheet and the magnitude of the total velocity in the z and y directions are slightly higher in the TF model than in the MFMS model. The current sheet is thinned sooner in the TF model than in the MFMS model, as shown in the animation of Figure 1 and in the top left panel of Figure 2. At the end of the laminar phase and during the plasmoid instability phase, comparing the evolution of the current sheet and total velocity fields remains difficult as the current sheet is unstable and fields change rapidly on short length scales. Therefore, further analysis has been performed and is presented in Figure 2.

Figure 2 shows the evolution of the thickness of the current sheet at a fixed $z = 2.45$ Mm (top left), the mean thickness of the whole current sheet (top right), the length of the current sheet (bottom left), and the maximum total velocity in the z direction $u_{tot,z}$ (bottom right) taken at the main reconnection site, for both the MFMS and TF models. To calculate the length at a fixed z , first, we locate the maximum of the magnitude of current for any $y \in [2.1, 2.3]$ Mm. Then, we consider its FWHM in the z direction to estimate the length. In our simulations, the maximum current is generally located at $y = L_0/2$. Similarly, the z component of the maximum total velocity at the reconnection site has been taken within the FWHM along the z -axis of the maximum current. Concerning the thickness at a fixed $z = 2.45$ Mm, a similar procedure as the estimation of the length of the current sheet has been

performed. First, we locate the maximum magnitude of the current for any y in the domain at a fixed $z = 2.45$ Mm. We choose the FWHM as it accurately represents the termination of the reconnection site for both the laminar and plasmoid instability phases. We extend these calculations to any $z \in [0.8, 3.2]$ Mm in order to calculate the evolution of the mean thickness and deviation of the current sheet.

Focusing on the left column of Figure 2, from 0 to approximately 25 s, for both the MFMS and TF models, the thickness at $z = 2.45$ Mm and length of the current sheet decrease drastically. This corresponds to a fast transition from the initial conditions to the beginning of the laminar phase leading to the formation of the current sheet. The initial thickness of the current sheet is $\lambda_\phi = 0.1L_0$ and the length $L_0 = 426$ km. In both the MFMS and TF models, from 0 to ~ 100 s, the thickness at $z = 2.45$ Mm of the current sheet decreases to ~ 25 km corresponding to the numerical length scale. Additionally, if we focus on the mean thickness of the current sheet (top right of Figure 2), it is clear that the thickness is larger in the MFMS model than in the TF model during the laminar phase. Consequently, the thickness of the current sheet in the TF model is reduced slightly faster than in the MFMS model, leading to higher velocities during the laminar regime, as shown in the bottom right of Figure 2. Note that there are no large disparities between the MFMS and TF models in the evolution of the length of the current sheet.

At $t \approx 100$ s, the plasmoid instability phase of the reconnection process starts. This phase is characterized by strong variation in the thickness of the current sheet, as shown in top left plot of Figure 2. In the MFMS model, we can clearly see that the thickness at $z = 2.45$ Mm increases around at $t = 200$ s from 25 to 80 km. Similarly in the TF model, a small variation in the thickness at $z = 2.45$ Mm is obtained around $t = 140$ s where the thickness increases from 25 to approximately 37 km. In general, at any time, the average size of the plasmoids appears to be slightly larger in the MFMS model than in the TF model meaning that the dilatation of the plasmoids during their formation is more important in the former than in the latter, as shown in the top right panel of Figure 2.

The plasmoid instability phase impacts the length of the current sheet that is associated with the maximum current J_x in both the MFMS and TF models (bottom left plot of Figure 2). Indeed, after $t \approx 100$ s, in both cases, strong variations in the length of the current sheet are obtained, but on average they decrease. This is because the presence of plasmoids breaks the initial current sheet formed during the laminar phase into multiple thinner current sheets. In summary, even during the plasmoid instability phase, on average, the mean frequency at which the plasmoids are formed and the length scales between them are similar between the MFMS and TF models.

At any time of the reconnection process, in both models, the maximum total velocity in the z direction $u_{\text{tot},z}$ increases, as illustrated in the bottom right of Figure 2. However, it is clear that the velocity is higher in the TF model than in the MFMS model, meaning that stronger flows are obtained in the former than in the latter, in both the laminar and plasmoid instability phases. Note that a similar result has been obtained in the y direction.

In summary, the average thickness of the current sheet and the size of the plasmoids appear to be slightly larger in the MFMS model than in the TF model, and reconnection with the TF model develops stronger flows than in the MFMS model. In this context, the presence of the helium species appears to only slightly impact the evolution of the current sheet as well as the flows. The length of the current sheet and the frequency at which the plasmoids are formed are similar between the two models. In the next sections, we will see that, even though these properties only slightly differ between the two models, the decoupling of the particles and composition of the plasma in the current sheet show large disparities, leading to different evolutions of the heating processes and temperatures.

5.2. Decoupling of the Particles and Velocity Fields

In this section, the decoupling of the particles and velocity fields are investigated. To do so, we focus on the z and y components of the velocity for each fluid separately. These correspond to the outflow and inflow directions of the magnetic reconnection, respectively.

The first four rows (starting from the top) of Figure 3 (Figure 4) represent the distribution of the y (z) component of the velocity of protons H^+ and the drift velocities with all the other particles in the MFMS model. The last two rows of the figures correspond to the velocity of protons H^+ and drift velocity between H and H^+ in the TF model. From left to right, the columns show the time evolution at times $t = 89$ s, $t = 282$ s, and $t = 327.5$ s, respectively.

During the laminar phase, the velocities of H^+ increase up to a maximum achieved at approximately 1 and 20 km s^{-1} (y and

z components) in both simulations. Note that the TF model seems to show slightly higher velocities, as described in Section 5.1. This maximum is reached at the end of the laminar phase, which corresponds to $t \approx 100$ s for both the MFMS and TF models. This corresponds to the time where the maximum length of the current sheet is achieved, as shown in Figure 2. In the first column of Figures 3 and 4, the drift velocities between particles are small compared to u_{y,H^+} and u_{z,H^+} , which implies that there is a large collisional coupling between species during the laminar phase. The decoupling between H^+ and He is the highest, as shown in panels (D) of Figure 3 and (F) of Figure 4. Neutral helium species moves slightly slower than H^+ by approximately 0.25 and 0.15 km s^{-1} in the y and z directions, respectively. Concerning the TF model, no significant decoupling between H and H^+ is seen.

In order to understand the evolution of the velocity fields, we have also calculated and analyzed the distributions of all the forces acting on each fluid involved in the MFMS or TF models, at different times. In the following, for the sake of simplicity, we briefly summarize them.

During the laminar phase, the initial structure of the magnetic field allows the development of a Lorentz force and leads to the formation of outflow and inflow velocities. The Lorentz force and gradient of pressure associated with H^+ are the dominant forces of the plasma in both the MFMS and TF models. Therefore, during the laminar phase, the dynamics of the reconnection process itself in the current sheet are dominated by these forces. This is also consistent with the fact that H^+ is the most dominant species in number and mass density in both the MFMS and TF models at that time. In the MFMS case, no drift velocities associated with H^+-H and H^+-He^+ occur as the species H^+ , H, and He^+ are highly coupled due to collisions. In other words, in each individual momentum equation associated with H and He^+ , the magnitude of the momentum exchange terms due to collisions with H^+ is large enough to highly couple the momentum equations associated with H, H^+ , and He^+ altogether. Similarly in the TF case, the fluids H and H^+ are highly coupled due to collisions during the laminar phase.

In contrast, in the MFMS model, the neutral helium species decouples from the other fluids. This drift at the current sheet is due to the fact that neutral He decouples from H^+ when the thickness of the current sheet thins down to the order of the mean free path between He and H^+ during the laminar phase, and neutral He is not dragged by collisions into the current sheet as quickly as H^+ or H. The decoupling between He and H^+ due to the lack of collisions is clearly illustrated in panel (D) of Figure 3 and in panel (C) of Figure 4. The fact that the decoupling between He and H^+ is stronger than that of other interactions is attributed to the collisional frequencies that involve neutral helium species, which are much smaller by more than 2 orders of magnitude than all the other collisional frequencies, as shown in Table 2 (for the initial conditions). These differences are attributed to the magnitude of the collision integrals at the kinetic level that leads to smaller collisional frequencies, as described with further details in Wargnier et al. (2022). This effect leads to slower velocities for neutral helium species with respect to H^+ , as illustrated in panel (D) of Figure 3 and panel (C) of Figure 4.

In the second and last columns of Figures 3 and 4 corresponding to the plasmoid instability phase, we note that drift velocities are increasing during the formation of plasmoids

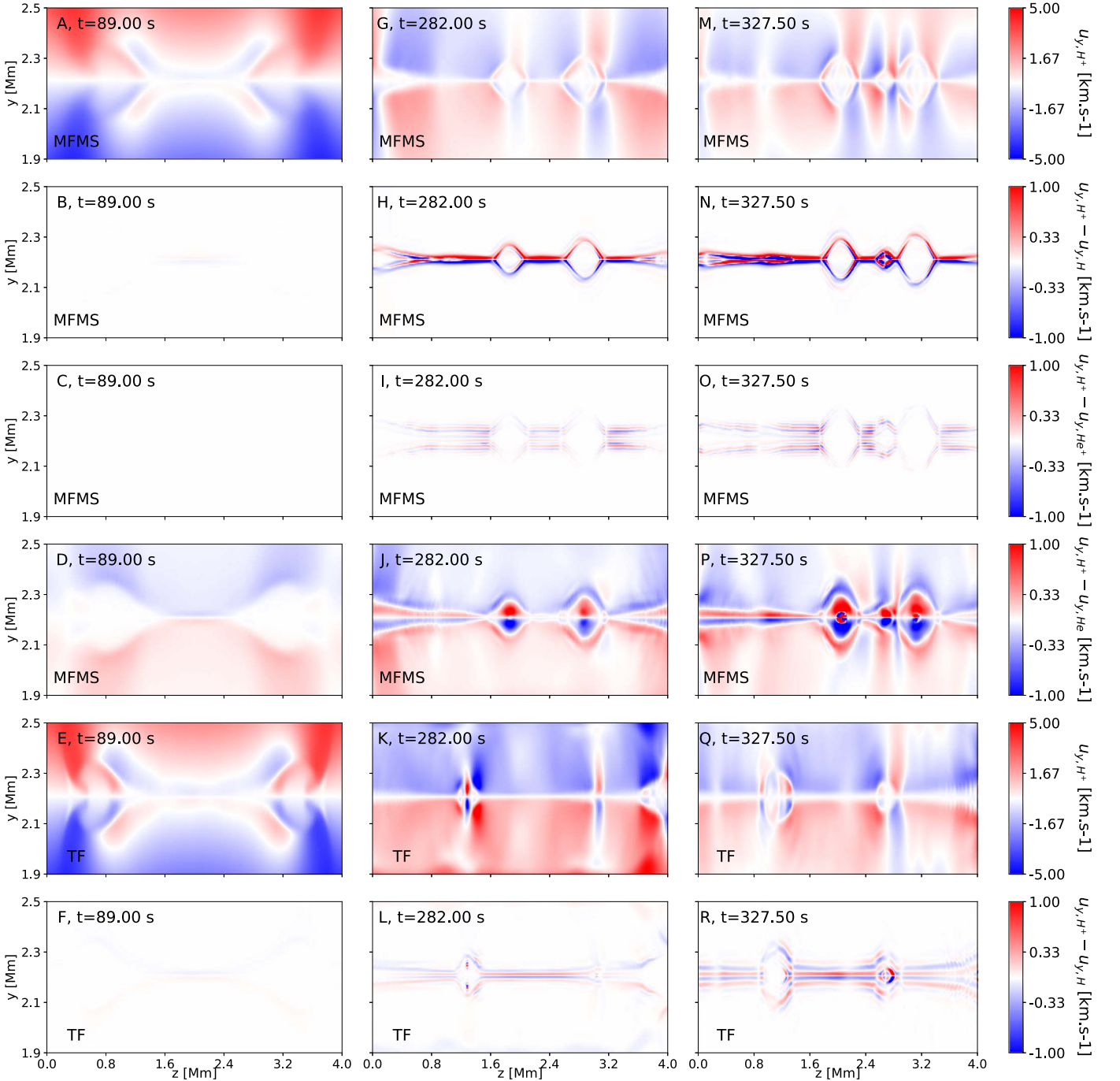


Figure 3. Distribution of the y component of the velocity of H^+ and drift velocities with other species in km s^{-1} at different times for the MFMS and TF models. From the first to the fourth row: distribution of the velocity u_{y,H^+} , the drift velocities $u_{y,H^+} - u_{y,H}$, $u_{y,H^+} - u_{y,He^+}$, and $u_{y,H^+} - u_{y,He}$ in the MFMS model, respectively. The last two rows corresponds to the distribution of the velocity u_{y,H^+} and the drift velocity $u_{y,H^+} - u_{y,H}$ in the TF model. From left to right: different times $t = 136$, $t = 278.5$, and 327.5 s are presented. An animation of this figure is available. The animation begins at $t = 0.5$ s and ends at 327.5 s. The real-time duration of the animation is 33 s. (An animation of this figure is available.)

for both the MFMS and TF models. This is also illustrated in the animations. When plasmoids are produced, the local velocity fields in opposite directions are generated due to a local reconnection of the magnetic field lines. It should be noted that the structure and evolution of the velocity of H^+ is similar for both the MFMS and TF models; however, the drift velocities differ between the two. In the case of the MFMS, the drift between H and H^+ is stronger at the boundary of plasmoids and inside the current sheet, reaching approximately

1 and 0.1 km s^{-1} for the y and z components, respectively, as we can see in panels (H) and (N) of Figure 3 and panels (G) and (L) of Figure 4. In the TF model, the drift velocity between H and H^+ is smaller than in the MFMS model by a factor of 3 and shows some oscillating pattern parallel to the current sheet, as shown in panel (R) of Figure 3. Similar to the decoupling between He and H^+ , the drift between H and H^+ develops during the plasmoid instability phase, as the current sheet thins down to the order of the mean free path (a few

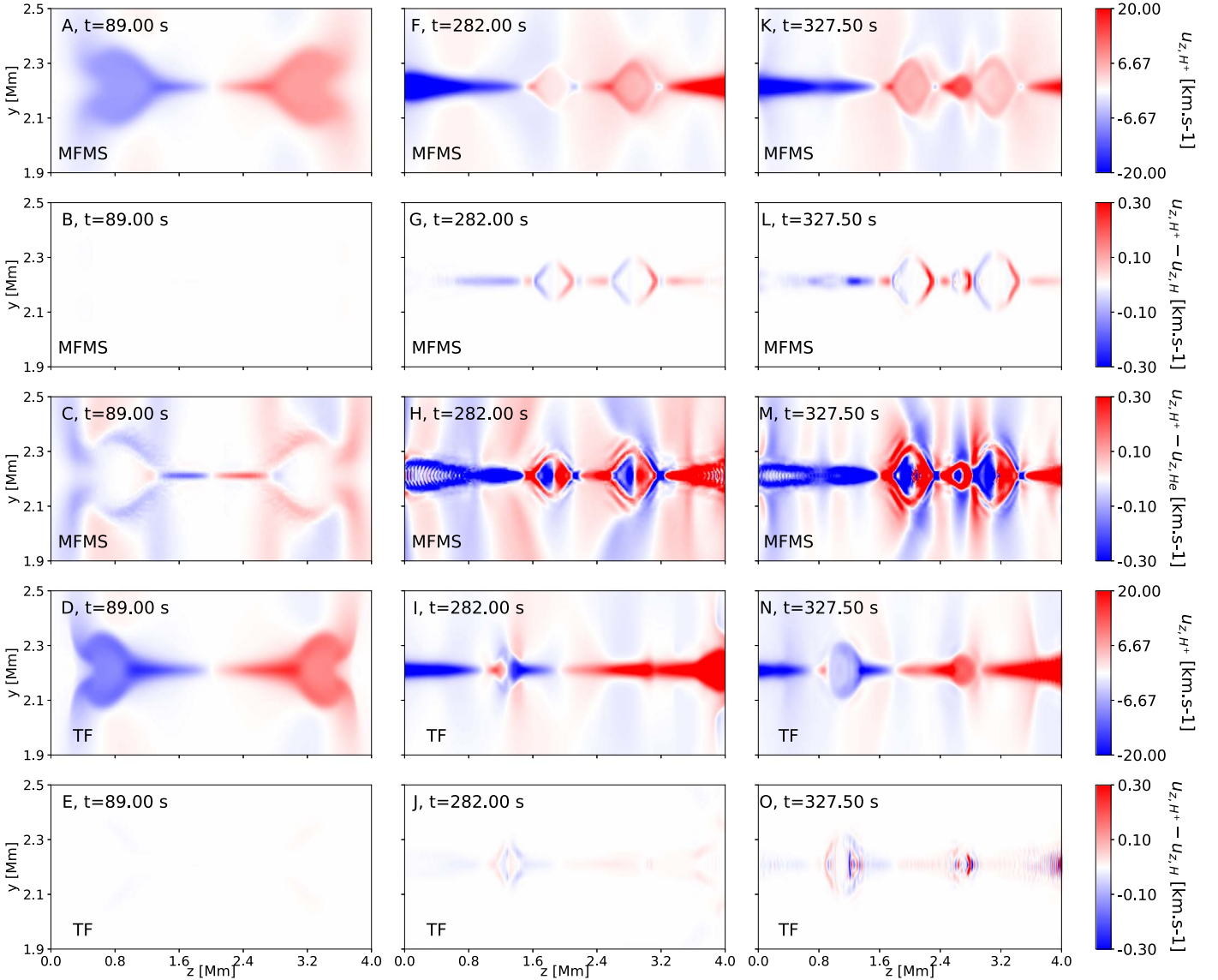


Figure 4. Similar layout as in Figure 3 for the z component of the velocities. Unlike Figure 3, the drift velocity between H^+ and He^+ is not shown as its magnitude is negligible compared to the other quantities. An animation of this figure is available. The animation begins at $t = 0.5$ s and ends at 327.5 s. The real-time duration of the animation is 33 s.

(An animation of this figure is available.)

kilometers corresponding to a few grid points) between H and H^+ , and neutral H does not collide enough with H^+ to be dragged into the current sheet as quickly as H^+ . This decoupling is consistent with the results obtained by Leake et al. (2012) and Leake & Linton (2013).

The drift between H and H^+ is higher in the MFMS model than in the TF model because the collisional frequency associated with $H-H^+$ interactions is smaller in the former than in the latter. As shown in Wargnier et al. (2022), the collisional frequencies are calculated from the products of (1) the collision integral associated with $H-H^+$ interaction, (2) H and H^+ number densities, and (3) thermal speed associated with $H-H^+$ interaction. In our chosen conditions, the number densities of H and H^+ in the MFMS model are smaller than those in the TF model due to the presence of helium species. Additionally, the temperature inside the current sheet is higher in the MFMS model than in the TF model, as shown later in Section 5.3, leading to a decrease in the collision integral

associated with $H-H^+$ interactions, as shown in Wargnier et al. (2022). These two effects contribute to the decrease in the collisional frequency associated with $H-H^+$ interactions in the MFMS model compared with the TF model. Note that, if the temperature increases, the thermal speed contributes the increase in the collisional frequency, as shown in the definition from Wargnier et al. (2022). However, in the chosen conditions and for $H-H^+$ interactions, this contribution is smaller than the contribution of the $H-H^+$ collision integral and number densities.

In panels (L) and (R) of Figure 3 and panels (J) and (O) of Figure 4, the oscillating pattern of the drift velocity between H and H^+ in the TF model is attributed to the spatial distribution momentum exchange term associated with $H-H^+$ interactions. These collisions compensate for the localized unbalance of the forces, i.e., the Lorentz force and pressure gradients, when the current sheet thins down to the mean free path between H and H^+ . A similar effect has been obtained in the distribution of

drift velocity between H^+ and He^+ in panel (O) of Figure 3 where the characteristic wavelength and magnitude of this pattern are much smaller than those of the drift between H and H^+ . However, this effect is attributed to two phenomena: the momentum exchange term associated with H^+-He^+ interactions in the MFMS model tries to compensate for the localized unbalance of forces (pressure gradients of H , H^+ , He , and He^+ and Lorentz forces acting on H^+ and He^+ separately) at much smaller spatiotemporal scales than those in the TF model. In addition, the ions experience a synchronized cyclotron-type motion along the magnetic field lines, also known as the ion-coupling effect, leading to a sinusoidal ion drift velocity distribution perpendicular to the magnetic field line, as described in further detail in Martínez-Sykora et al. (2020). Note that the z component of the drift velocity associated with H^+-He^+ interactions is negligible. Consequently, the distribution of the latter has not been shown here.

As in the laminar phase, the decoupling between He and H^+ remains important due to the lack of collisions between the two species. This drift velocity is high both inside the current sheet and plasmoids. The maximum drift velocity between He and H^+ reaches more than 1 km s^{-1} and 0.3 km s^{-1} in the y and z directions, respectively. We can also notice some internal structure of the drift velocity inside the plasmoids (panels (J) and (P) of Figure 3 and panels (H) and (M) of Figure 4). The wavy pattern on the left of panels (H) and (M) is not a real phenomenon and is caused by the numerical scheme that uses a high-order stencil.

5.3. Multifluid Heating Processes

5.3.1. Heating Processes due to Departure in Velocities

In order to analyze the heating processes and identify the type of collisions mainly responsible for the increase in temperature, we focus on the dominant heating terms due to drift velocities $Q_{\alpha\mathcal{I},\alpha'\mathcal{I}'}^{u,\text{col}}$ in both models MFMS and TF. As explained in Section 2.3, the heating terms associated with the drift velocities are not adiabatic terms and can increase the total thermal energy of the plasma. Therefore, the heating processes for both the MFMS and TF models could be strongly connected to the structure of the drift velocities, which have been investigated in Section 5.2.

Under the chosen thermodynamic conditions presented in Section 4, the electron thermal conduction and the terms associated with ionization or recombination processes $Q_{\alpha\mathcal{I}}^{\text{ion}}$ or $Q_{\alpha\mathcal{I}}^{\text{rec}}$ have negligible impact on the heating processes, in both the MFMS and TF models. Indeed, as described in Section 2, the heating terms associated with ionization or recombination processes for any $\alpha\mathcal{I} \in \mathcal{H}$ do not contribute to the total thermal energy of the plasma (apart from the radiative losses term). Thus, they do not contribute to the current sheet's temperature increase. In all thermal energy equations, the magnitude of these terms is negligible compared to the thermalization terms due to collisions as the ionization and recombination timescales are bigger than collisional timescales, as described in Section 4.2 and also in Section 5.4.1.

Figure 5 presents the distribution of the rate of the heating terms $Q_{\alpha\mathcal{I},\alpha'\mathcal{I}'}^{u,\text{col}}$ in a 1D cut of the current sheet located at $z = 2.45 \text{ Mm}$ for all the possible interactions involved in both the MFMS (top row) and TF (middle row) models at different times $t = 11.5 \text{ s}$ and $t = 28.5 \text{ s}$ from left to right. Note that these times correspond to a different stage of the laminar phase. The

rates are calculated by dividing the heating terms, produced by drift velocities, by the total thermal energy $e_{\text{tot}}^\alpha = \sum_{\alpha\mathcal{I} \in \alpha} e_{\alpha\mathcal{I}}$, $\alpha \in \{\mathcal{M}, \mathcal{M}_{\text{TF}}\}$. We also show the distribution of the temperatures of each species in the MFMS and TF models (bottom row) at $z = 2.45 \text{ Mm}$. Note that an animation of this figure is available.

At the beginning of the laminar phase in the MFMS model, it is clear that the heating processes produced by the drifts between H^+ and He , and H and He dominate in the current sheet, as observed in panel (A) of Figure 5. This effect is consistent with Section 5.2 showing that the drift velocities between neutral helium and hydrogen species are much higher than any other interactions during the laminar phase. Additionally, the heating due to collisions between electrons and all heavy species (ohmic collisions) is of the same order of magnitude as H^+-He and $H-He$ interactions but localized around the current sheet. The heating due to the drift between H^+ and H is not negligible in the current sheet. Still, it is much lower than those due to other interactions (panel (A) of Figure 5), which is also consistent with the magnitude of the drift velocity in Section 5.2. In the TF case, the heating produced by the drift between electrons and heavy species (H and H^+) is dominant, as shown in panel (B). Additionally, the latter is slightly higher in magnitude as the heating is produced by the drift between electrons and heavy species in panel (A) (black dashed line in panel (A)). However, if we sum all the heating terms of panel (A) and compare it with the sum of all the heating terms in panel (B), it is clear that the total heating produced by velocity drifts is higher, by approximately a factor 2, in the MFMS model than in the TF model due to the heating terms $Q_{H,He}^{u,\text{col}} + Q_{He,H}^{u,\text{col}}$ and $Q_{H^+,He}^{u,\text{col}} + Q_{He,H^+}^{u,\text{col}}$.

At a later time of the laminar phase, corresponding to the second column of Figure 5, the temperatures of all species in the MFMS model increase and are higher than those in the TF model. The temperature achieves its maximum at the center of the current sheet at $27,000 \text{ K}$ in the MFMS model. In contrast, in the TF model, the temperature is approximately $19,000 \text{ K}$ at the center of the current sheet (panel (F)). By comparing panels (A) and (D), the magnitude of the heating terms due to collisions associated with interactions $H-He$, H^+-He , and electrons-heavy species increase in time inside the current sheet. This increase is attributed to drift velocities increasing with time during the laminar phase. Similarly, if we sum all the heating terms in panels (A) and (B), the sum of all the heating terms is higher in the MFMS model than in the TF model. Consequently, temperatures inside the current sheet are higher in the MFMS model than in the TF model. Note that temperatures of all species are equal during the laminar phase in both models.

Figure 6 shows the heating rates due to the drift velocities $Q_{\alpha\mathcal{I},\alpha'\mathcal{I}'}^{u,\text{col}} + Q_{\alpha'\mathcal{I}',\alpha\mathcal{I}}^{u,\text{col}}$, $(\alpha\mathcal{I}, \alpha'\mathcal{I}') \in \mathcal{M}^2$ or $\mathcal{M}_{\text{TF}}^2$ divided by the total thermal energy and the temperature of protons T_{H^+} , for the MFMS (first five rows) and TF (last two rows) models, at different times of the simulation corresponding to the plasmoid instability phase. From left to right, the columns correspond to times $t = 210, 250$ and 282.5 s , respectively. Higher temperatures are reached inside the current sheet and plasmoids than during the laminar phase, as shown in panels (E), (L), (S), (G), (N), and (U) of Figure 6 by comparing with the temperatures presented in Figure 5.

Additionally, higher temperatures are reached in MFMS than in TF, as illustrated in panels (E), (L), and (S) in comparison

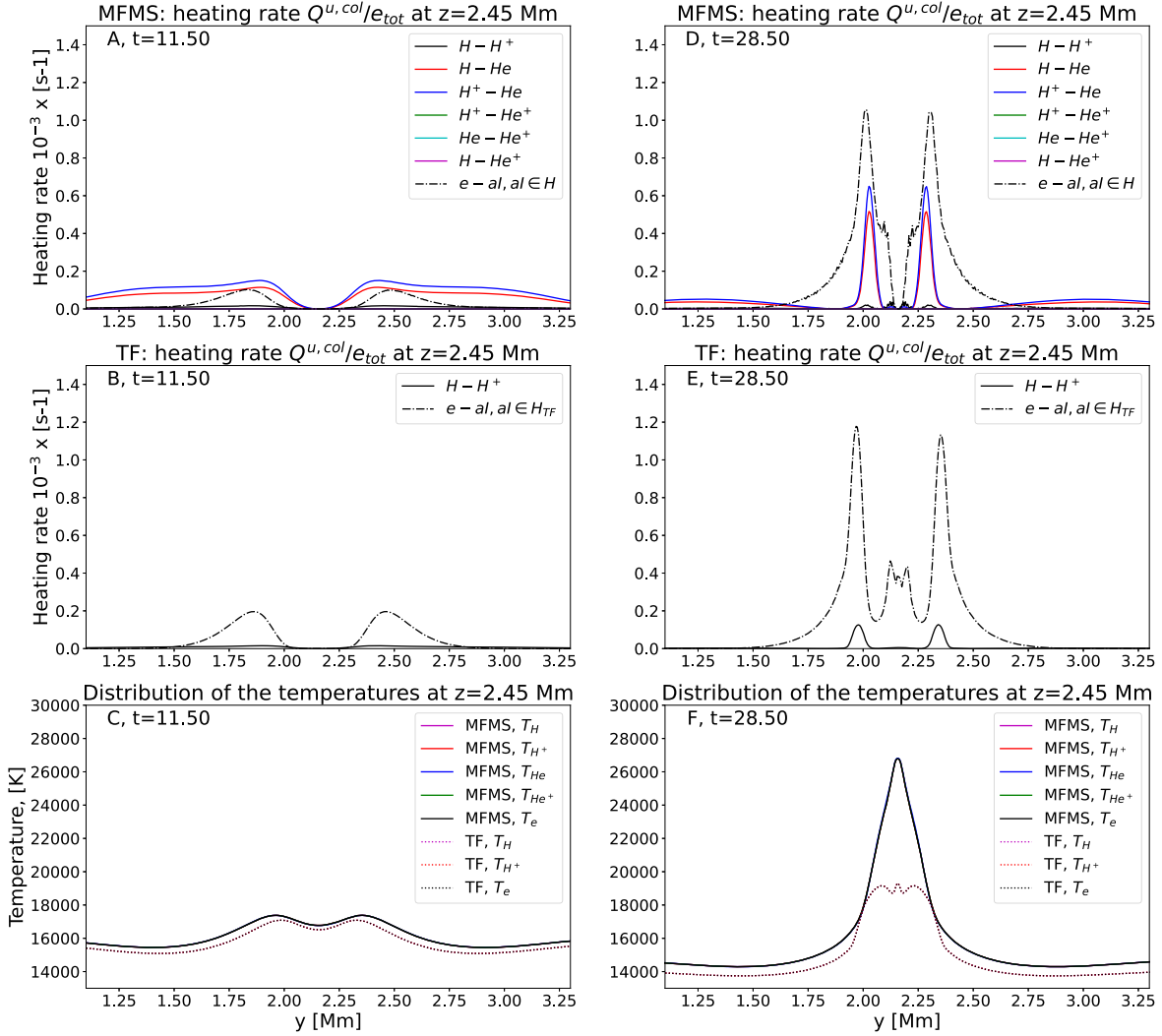


Figure 5. Distribution of the rates of the heating terms $Q_{\alpha I, \alpha' I'}^{u, col} + Q_{\alpha' I', \alpha I}^{u, col}$, $(\alpha I, \alpha' I') \in \mathcal{M}^2$ or \mathcal{M}_{TF}^2 associated with the drift velocities divided by the total thermal energy $e_{tot} = \sum_{\alpha I \in \mathcal{M}} e_{\alpha I}$ in s^{-1} (top row for the MFMS model and middle row for the TF model) and temperatures of each particles (bottom row) along the z -axis in the current sheet at position $y = L_0/2$ in both the MFMS and TF models, respectively. From left to right: distributions at different times $t = 11.5$ s and $t = 28.5$ s corresponding to the laminar phase. Note that the vertical axis ranges from 0 to $1.4 \times 10^{-3} s^{-1}$. An animation of this figure is available. The animation begins at $t = 0.5$ s and ends at 50 s. The real-time duration of the animation is 10 s.

(An animation of this figure is available.)

with panels (G), (N), and (U) of Figure 6. Indeed, in TF, the temperatures achieve a maximum of 35,000 K, whereas in MFMS the temperatures can reach up to approximately 50,000 K. In TF, this temperature is reached with the H and H^+ drift heating (panels (F), (M), and (T)). These panels show that the rate of the heating terms ranges from $10^{-2.8}$ to $10^{-3} s^{-1}$ inside the current sheet and plasmoids, increasing the temperature T_{H^+} from 22,000 K (panel (G)) to 30,000 K. In the plasmoid located at $z \approx 1.5$ Mm, the temperature achieves a maximum of 35,000 K due to the $H-H^+$ drift (panel (U)).

In the MFMS model, as many species and interactions are involved, the heating produced by drift velocities is more complex to interpret than in the TF model and requires the analysis of several components of the heating terms during the plasmoid instability phase.

First, if we compare panels (A), (H), and (O) with (F), (M), and (T), the rate associated with the heating terms due to the drift between H and H^+ is much higher in the MFMS model than in the TF model. The disparity can reach up to 1 order of

magnitude in some regions of the current sheet. For example, at $z \approx 1.6$ or $z \approx 3.2$ Mm of panel (O), the rate achieves a maximum at $10^{-2} s^{-1}$. Therefore, the temperature T_{H^+} increases in these regions from 30,000 K to $\sim 50,000$ K between $t = 210$ and $t = 282.5$ s, (panels (E), (L), and (S)). Even though most of the heating comes from the H and H^+ collision, the heating due to the H^+ and He^+ collision is not negligible at $z \approx 1.6$ or $z \approx 3.2$ Mm (panel (R)). This last heating rate is approximately $10^{-3.1} s^{-1}$ (panels (D), (K), and (R)).

Focusing on the formation of the plasmoid located at $z \approx 1.9$ Mm in panels (E), (L), and (S) of Figure 6, one can notice that the thickness of this plasmoid increases. This dilation is the consequence of the balance of the thermal pressure of the plasma inside the current sheet that increases with respect to the magnetic pressure, which is constant. Therefore, during this dilation, the temperature inside the plasmoid is constant, and $\sim 50,000$ K, while its thickness increases from ~ 0.08 to ~ 0.2 Mm. Therefore, the dilation process of the

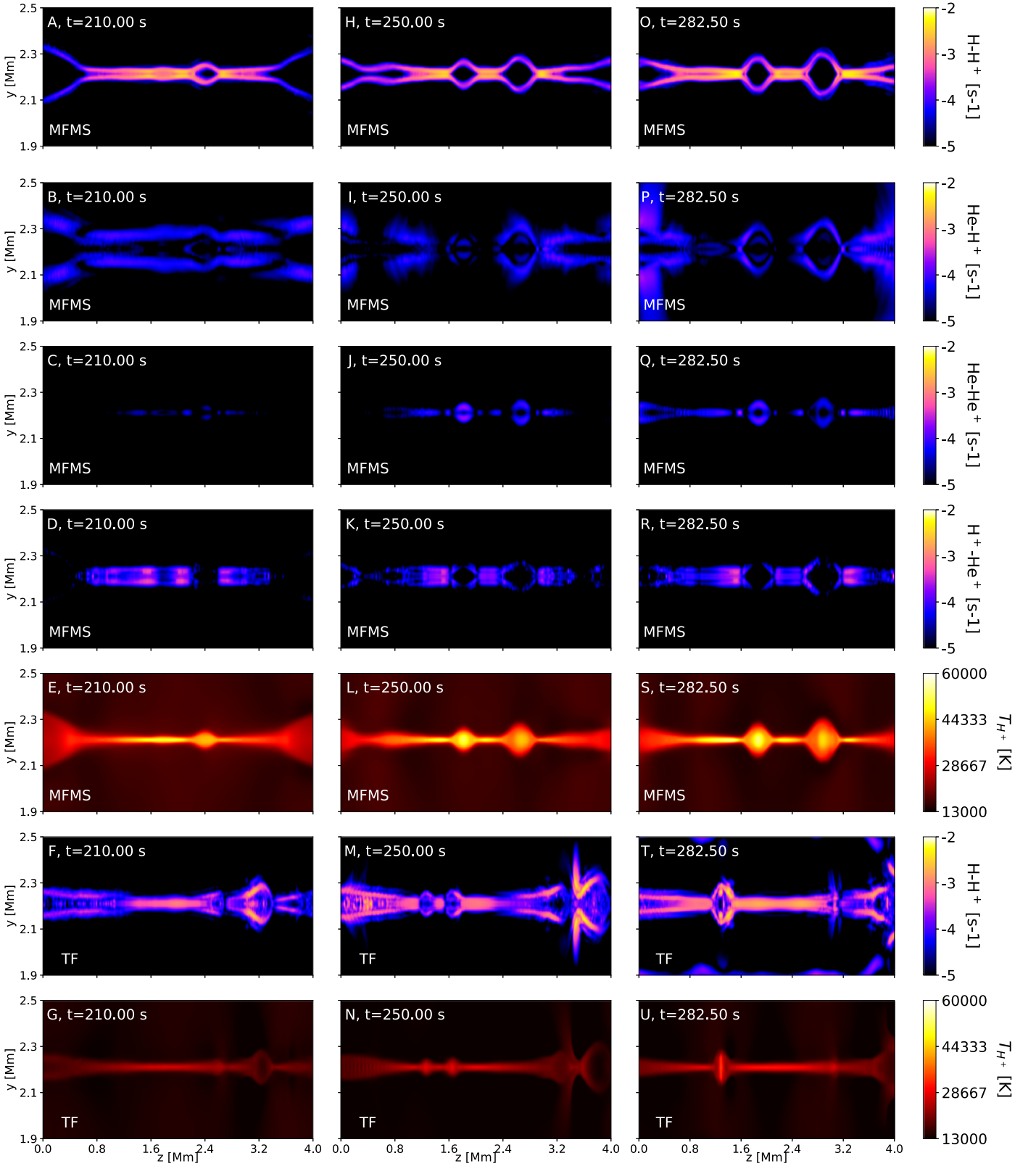


Figure 6. From top to bottom: for any $(y, z) \in [1.9, 2.5] \times [0, 4]$ Mm, distribution of the decimal logarithm of the rates of the heating terms $Q_{\alpha\mathcal{I}, \alpha'\mathcal{T}}^{u, \text{col}, S}$, $(\alpha\mathcal{I}, \alpha'\mathcal{T}) \in \mathcal{M}^2$ divided by the total thermal energy $e_{\text{tot}} = \sum_{\alpha\mathcal{I} \in \mathcal{M}} e_{\alpha\mathcal{I}}$ in s^{-1} in the MFMS model, the temperature of H^+ in the MFMS model, the decimal logarithm of the heating terms $Q_{\alpha\mathcal{I}, \alpha'\mathcal{T}}^{\text{col}}$, $(\alpha\mathcal{I}, \alpha'\mathcal{T}) \in \mathcal{M}_{\text{TF}}^2$ divided by the total thermal energy $e_{\text{tot}} = \sum_{\alpha\mathcal{I} \in \mathcal{M}_{\text{TF}}} e_{\alpha\mathcal{I}}$ in s^{-1} in the TF model, and the temperature of H^+ in the TF model. The other heating terms have not been shown here as their magnitudes are negligible compared to the other terms. From left to right: distributions at different times $t = 210, 250$, and 282.5 s corresponding to different stages of the plasmoid instability phase. An animation of this figure is available. The animation begins at $t = 0.5$ s and ends at 327.5 s. The real-time duration of the animation is 33 s.

(An animation of this figure is available.)

thermodynamic system defined as the volume of plasma located inside the plasmoid at $z \approx 1.9$ Mm between $t = 210$ and $t = 282.5$ s is not adiabatic. However, if we look at panels (A), (H), and (O) or (D), (K), and (R), it is clear that the heating terms due to the drift between H and H^+ or H^+ and He^+ are negligible inside the plasmoid. Therefore, one has to focus on other heating sources inside the plasmoids to explain the nonadiabaticity of the dilatation.

Indeed, the heating due to the friction between He and He^+ is not negligible inside the plasmoid, as shown in panels (C), (J), and (Q) of Figure 6. In panel (J), at $z \approx 1.9$ Mm, the heating rate associated with He– He^+ collisions is approximately equal to $10^{-3.4} \text{ s}^{-1}$, which allows maintaining the plasma temperature inside the plasmoid to 50,000 K during the dilatation. The cooling rate associated with the adiabatic expansion of the plasmoids is negligible compared to this heating rate due to He– He^+ collisions ($\approx 10^{-4.2} \text{ s}^{-1}$). The temperature of the second plasmoid located at $z \approx 3$ Mm is slightly lower than the other plasmoid and ranges from 35,000 to 40,000 K. This is because the initial plasma temperature in the current sheet where this plasmoid is initially formed is lower than the initial plasmoid temperature located at $z \approx 1.9$ Mm. Indeed, during the plasmoid instability phase, the temperature distribution is not uniform along the z -axis leading to some variations in the temperature of the formed plasmoids.

Furthermore, the heating rate due to He and He^+ collisions in the plasmoid at $z \approx 3$ Mm is lower than at $z \approx 1.9$ Mm, and approximately equal to 10^{-4} s^{-1} , as we can see in panel (J) of Figure 6. The heating due to the friction between He and H^+ slightly contributes to the heating of the plasmoids, as we can see in panels (B), (I), and (P). Note that this contribution is not included in the TF model. Thus, during the expansion of the plasmoids, the temperature inside the plasmoids decreases and diffuses with time.

In summary, the temperature is higher in the MFMS model than in the TF model both during the laminar (with temperatures of 30,000 K and 20,000 K for the MFMS and TF models, respectively) and plasmoid instability phases (65,000 K and 35,000 K for the MFMS and TF models, respectively). Consequently, in the MFMS case and for the chosen initial thermodynamic conditions, the plasma reaches a sufficient temperature inside the current sheet to eventually ionize helium species rapidly. During the plasmoid instability phase, the main heating process is due to the collisions between H and H^+ . It allows increasing the temperature inside the current sheet from 30,000 to 50,000 K. Then, plasmoids are produced and expanded following a nonadiabatic process. In this context, neutral helium is rapidly ionized (as described with further details in Section 5.4) and collides with all the other particles, in particular He, inside the plasmoids. It allows the maintenance of the temperature of the plasmoids at 50,000 K (for the plasmoid located at $z = 1.8$ Mm). A maximum temperature of 65,000 K is achieved inside the plasmoids at a later time of the plasmoid instability phase.

5.3.2. Decoupling of the Temperatures in the MFMS Model

In this section, we focus only on the MFMS model at a later time of the plasmoid instability phase. Indeed, these effects appear to be out of reach in the TF model. In the MFMS model, our previous results from Section 5.3.1 have shown that most of the temperatures are in equilibrium during the laminar and plasmoid instability phase. This is because the thermalization

terms for any possible interactions $Q_{\alpha\mathcal{I},\alpha'\mathcal{I}'}^{T,\text{col}}$, $(\alpha\mathcal{I}, \alpha'\mathcal{I}') \in \mathcal{M}^2$ have larger magnitudes than any other heating terms such as $Q_{\alpha\mathcal{I},\alpha'\mathcal{I}'}^{u,\text{col}}$, $(\alpha\mathcal{I}, \alpha'\mathcal{I}') \in \mathcal{M}^2$ or Q_e^{spitz} . In other words, the characteristic timescale of the thermalization terms range from 10 s to just a few seconds whereas the heating terms associated with drift velocities exceed 100 s, as shown in Figure 6.

Departures in temperature occur for a couple of species $(\alpha\mathcal{I}, \alpha'\mathcal{I}') \in \mathcal{M}^2$ if the rate associated with all the heating processes of particles $\alpha\mathcal{I}$ becomes much higher than the rate of the thermalization term $Q_{\alpha\mathcal{I},\alpha'\mathcal{I}'}^{T,\text{col}}/e_{\alpha\mathcal{I}}$. In other words, for any $(\alpha\mathcal{I}, \alpha'\mathcal{I}') \in \mathcal{M}^2$, neglecting the electron thermal conduction and radiative losses, this condition can be written as

$$\frac{Q_{\alpha\mathcal{I},\alpha'\mathcal{I}'}^{T,\text{col}}}{e_{\alpha\mathcal{I}}} \ll \frac{1}{e_{\alpha\mathcal{I}}} \left(\sum_{\alpha^*\mathcal{I}^* \in \mathcal{M}} Q_{\alpha\mathcal{I},\alpha^*\mathcal{I}^*}^{u,\text{col}} \right) = \frac{Q_{\alpha\mathcal{I}}^{u,\text{col}}}{e_{\alpha\mathcal{I}}}. \quad (21)$$

In order to highlight the thermal decoupling effects occurring during the reconnection process, we focus only on neutral helium. Neutral helium shows strong thermal decoupling effects due to the high decoupling in collisions with other species, as shown in the previous sections. Figure 7 shows the rate $Q_{He}^{u,\text{col}}/e_{He}$ distribution compared with all the rates associated with the thermalization terms $Q_{He,\alpha\mathcal{I}}^{T,\text{col}}/e_{He}$, $\alpha\mathcal{I} \in \mathcal{M}$ at times $t = 307.5$ s, and $t = 314.5$ s in the current sheet at $y = L_0/2$. On top of that, we also show the distributions of all the temperatures (panels (B) and (E)) as well as the differences in temperature $\Delta T = T_{He} - T_{\alpha\mathcal{I}}$, $\alpha\mathcal{I} \in \mathcal{H}$ with respect to the neutral helium temperature T_{He} (panels (C) and (F)).

First, if we focus on the plasmoid located at $z \approx 2$ Mm at $t = 307.5$ s, in panel (A), the rate of the total heating term $Q_{He}^{u,\text{col}}/e_{He}$ is slightly higher than the rates $Q_{He,H^+}^{T,\text{col}}/e_{He}$ and comparable to $Q_{He,He^+}^{T,\text{col}}/e_{He}$. After a few seconds, corresponding to panel (D) of Figure 7, the rate of the total heating term $Q_{He}^{u,\text{col}}/e_{He}$ increases drastically (500% in 7 s) and becomes much larger than the rates of the thermalization terms $Q_{He,H^+}^{T,\text{col}}/e_{He}$ and $Q_{He,He^+}^{T,\text{col}}/e_{He}$ and stay comparable to $Q_{He,He^+}^{T,\text{col}}$. In this framework, the condition in Equation (21) is satisfied for the couples of species (He, H^+) and (He, H). This leads to a fast and strong thermal decoupling where the departures in temperatures $T_{He} - T_{H^+}$ and $T_{He} - T_H$ achieve a maximum at ≈ 3000 K, occurring in just a few seconds, at the center of the plasmoid.

During the reconnection process, thermal decoupling effects can be stronger leading to a neutral helium temperature that can become much larger and reach up to 90,000 K where other species temperatures stay at 70,000 K. Note that this effect occurs at later time of the plasmoid instability phase. Additionally, a small temperature decoupling is seen in neutral hydrogen, as illustrated with the blue line in panels (C) and (F). However, this effect remains smaller than temperature decoupling effects associated with neutral helium.

5.4. Evolution of the Composition

5.4.1. Evolution of the Ionization Levels in the MFMS and TF Models

Figures 8 and 9 (first two rows) show the distribution of the total ionization fraction of the MFMS and TF models. Figure 8 is a cut in the middle of the current sheet at $y = L_0/2$ during the laminar phase (on the left) and plasmoid instability phase (on the right). In Figure 8, the distributions of the ionization fraction of hydrogen and helium species are shown. Figure 10 has the same layout as Figure 9 but for the distribution of the

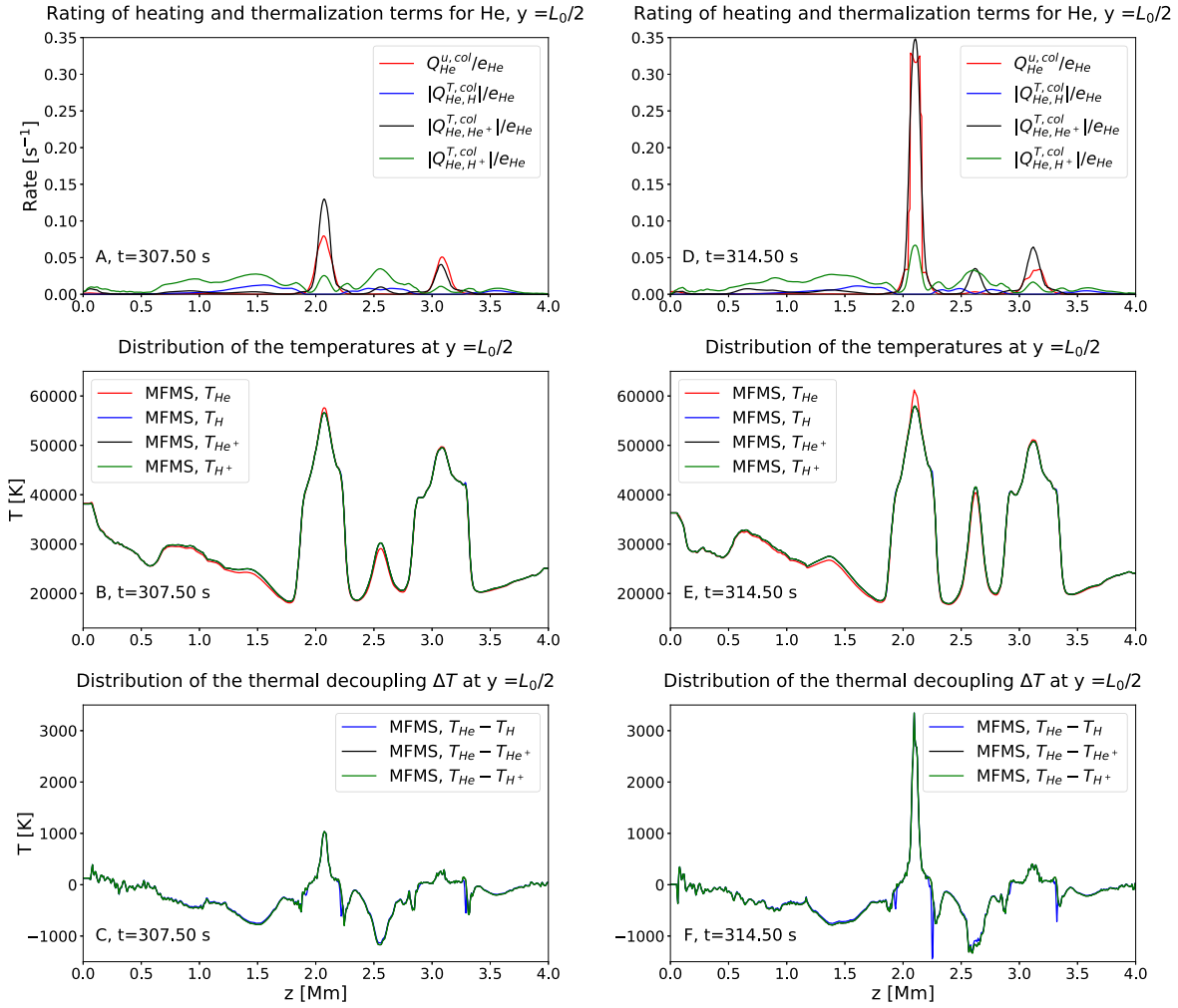


Figure 7. From top to bottom: distribution along the z -axis at $y = L_0/2$ of the rates of the total heating term $Q_{\text{He}}^{u,\text{col}}/e_{\text{He}}$ and all the thermalization terms $Q_{\text{He},\alpha Z}^{T,\text{col}}/e_{\text{He}}$, with $\alpha Z \in \mathcal{M}$, distribution of all the temperatures, and distribution of temperature differences ΔT with respect to T_{He} in the current sheet at position $y = L_0/2$ for the MFMS model. From left to right: distributions at different times $t = 307.5$ s and $t = 314.5$ s.

ionization and recombination frequencies $\nu_{\text{H},\text{H}^+}^{\text{ion}}$, $\nu_{\text{H}^+,\text{H}}^{\text{rec}}$ for the MFMS and TF models, and $\nu_{\text{He},\text{He}^+}^{\text{ion}}$ for the MFMS model. These frequencies allow for the assessment of the evolution of ionization and recombination effects, and the composition of the plasma is altered during the reconnection process. The recombination frequency $\nu_{\text{He}^+,\text{He}}^{\text{rec}}$ is negligible and much smaller than the other ionization and recombination frequencies; thus, it is not shown here.

During the laminar phase, represented in the first column of Figures 9 (panels (A) and (B)) and 10 (panels (A) to (E)), and left plot of Figure 8, the ionization level is increasing in the current sheet for both the MFMS and TF models due to the ionization of the hydrogen species. Indeed, the ionization frequency $\nu_{\text{H},\text{H}^+}^{\text{ion}}$ in the current sheet, in both the MFMS and TF models, is higher by more than 1 order of magnitude than the recombination frequency $\nu_{\text{H}^+,\text{H}}^{\text{rec}}$, as shown in Figure 10. Furthermore, the recombination frequency $\nu_{\text{H}^+,\text{H}}^{\text{rec}}$ in the MFMS model (panel (B)) is lower than in the TF model (panel (E)). This leads to an ionization level that is much higher in the MFMS model (ranging from 85% to 95%) than in the TF model (ranging from 70% to 80%) during the laminar phase, as shown on the left of Figure 8. These disparities obtained in the ionization and recombination frequencies between the two models are attributed to the difference in temperature of the

plasma in the current sheet during the laminar phase. Indeed, as described in Section 5.3, the presence of the helium species that collides with the hydrogen species in the MFMS model leads to higher temperatures in the current sheet than in the TF model. This increase in temperature gives rise to a larger hydrogen ionization in the MFMS model than in the TF model during the laminar phase.

The ionization levels in plasmoids are drastically increasing for both the MFMS (right panel in Figure 8) and TF models compared to the laminar phase (left panel). In the TF model, we can distinguish three plasmoids located at $y = 1.5$ Mm, 3.1 Mm, and 3.7 Mm, and, in the MFMS model, two plasmoids located at $y = 1.9$ Mm and 3 Mm. In the TF model, at the middle of the plasmoid located at $y = 1.5$ Mm, the ionization level increases up to more than 98%. This is attributed to a local increase in the temperature inside plasmoids, giving rise to an increase in H^+ due to ionization process, as illustrated in panel (I) of Figure 10.

In the MFMS model, the friction of the hydrogen species with neutral helium allows a higher temperature level in the plasmoids than in the TF model during the plasmoid instability phase, as described in Section 5.3. This level of temperature is high enough to ionize helium, as illustrated in Figure 8 by the large increase in the black dotted line. This is also illustrated in

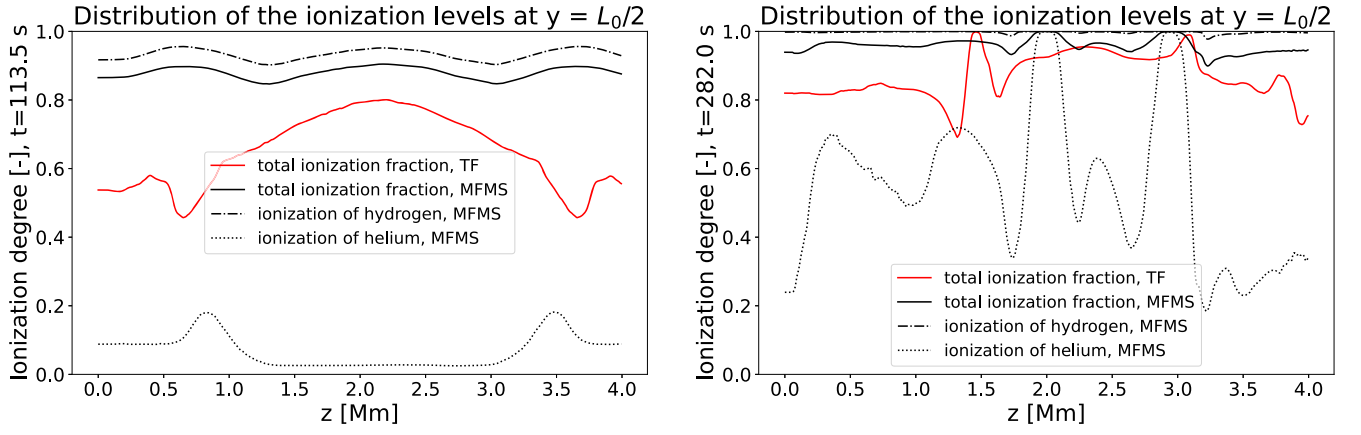


Figure 8. Distribution of the total ionization fraction for both the MFMS and TF models, ionization of the hydrogen and helium species in the MFMS model in the middle of the current sheet at position $y = L_0/2$ at times $t = 113.5$ s (left) and $t = 282$ s (right), respectively. The solid black, dashed black, and dotted black lines correspond to the total ionization fraction, the ionization of hydrogen species $x_{\text{H}^+} = n_{\text{H}^+}/(n_{\text{H}^+} + n_{\text{H}})$, and the ionization of helium species $x_{\text{He}^+} = n_{\text{He}^+}/(n_{\text{He}^+} + n_{\text{He}})$ for the MFMS model, respectively. The solid red line corresponds to the total ionization fraction in the TF model. An animation of this figure is available. The animation begins at $t = 0.5$ s and ends at 327.5 s. The real-time duration of the animation is 33 s.

(An animation of this figure is available.)

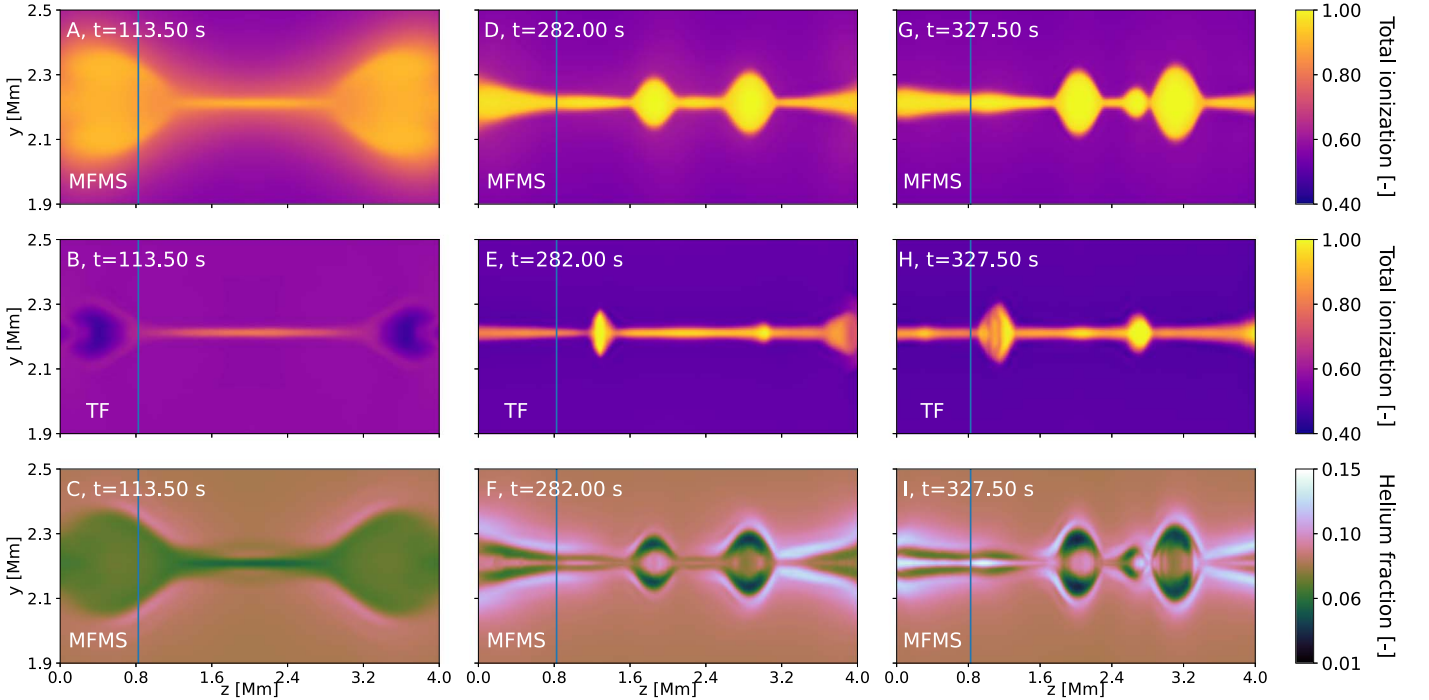


Figure 9. Distribution of the total ionization fraction in the TF (first row) and MFMS (second row) models, molar fraction of helium species ($n_{\text{He}} + n_{\text{He}^+})/(\sum_{\alpha \in \mathcal{M}} n_{\alpha})$ in the MFMS model, at different times $t = 113.5$ s, $t = 282$ s, and $t = 327.5$ s for any $(y, z) \in [1.8, 2.6] \times [0, L_0]$ Mm (from left to right), respectively. The vertical line corresponds to $z = 0.825$ Mm. An animation of this figure is available. Unlike the figure, the animation has four panels. The first three are identical to the figure, but the far right panel shows the molar fraction of hydrogen species $(n_{\text{H}} + n_{\text{H}^+})/(\sum_{\alpha \in \mathcal{M}} n_{\alpha})$. The animation begins at $t = 0.5$ s and ends at 327.5 s. The real-time duration of the animation is 33 s.

(An animation of this figure is available.)

panels (H) and (M) of Figure 10 where we can clearly see that $\nu_{\text{He}^+, \text{He}}^{\text{ion}}$ increases drastically, especially in the core of plasmoids. At this moment, a self-sustaining mechanism occurs. Indeed, when He^+ species are produced, they collide with both H^+ and He , as described in Section 5.3. In this context, an additional heating process occurs due to collisions involving He^+ . This effect will slightly increase the temperature at the center of the plasmoid, leading to even more He^+ due to the ionization process. This is characterized by the

increase in $\nu_{\text{He}^+, \text{He}}^{\text{ion}}$ in the core of plasmoids, as illustrated in panels (H) and (M) of Figure 10.

5.4.2. Chemical Fractionation in the MFMS Model

In this section, we focus only on the MFMS model and the chemical fractionation between the helium and hydrogen species during the reconnection process. In Figure 9 (last row), the distributions of the helium species molar fraction at different times, corresponding to the laminar and plasmoid

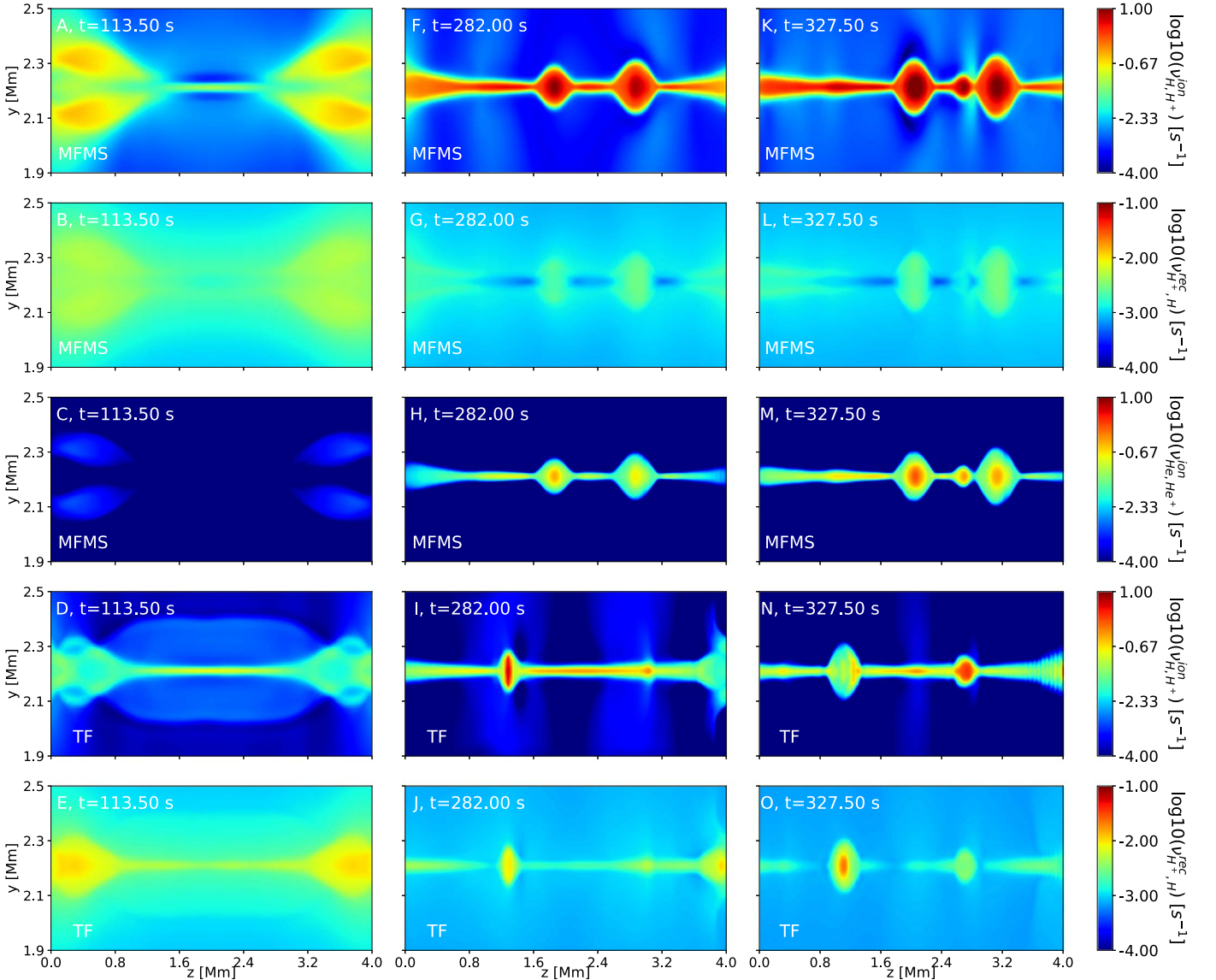


Figure 10. Distribution of the decimal logarithm of the ionization and recombination frequencies in s^{-1} of the MFMS (first three rows) and TF (last two rows) models at different times $t = 113.5$ s, $t = 282$ s, and $t = 327.5$ s for any $(y, z) \in [1.8, 2.6] \times [0.4, 4]$ Mm (from left to right), respectively. From top to bottom: distribution of ν_{H,H^+}^{ion} , $\nu_{H^+,H}^{\text{rec}}$, and $\nu_{\text{He,He}^+}^{\text{ion}}$ in the MFMS model, and distribution of ν_{H,H^+}^{ion} , $\nu_{H^+,H}^{\text{rec}}$ in the TF model. Note that the distribution of $\nu_{\text{He,He}^+}^{\text{rec}}$ is not shown as the magnitude is negligible and much smaller than $10^{-4} s^{-1}$. An animation of this figure is available. The animation begins at $t = 0.5$ s and ends at $t = 327.5$ s. The real-time duration of the animation is 33 s.

(An animation of this figure is available.)

instability phase, is shown. The molar fraction is defined as $(n_{\text{He}} + n_{\text{He}^+}) / (\sum_{a \in \mathcal{M}} n_a)$.

During the laminar phase, in the MFMS model, the helium species molar fraction (panel (C) of Figure 9) decreases in the current sheet (from 7.9% to 6%). Additionally, we also notice a small increase in the helium species molar fraction at the boundary of the current sheet close to the outflow regions. Indeed, as helium is not ionized, these effects are attributed to the accumulation of neutral helium species, which are decoupled from the hydrogen species nearby the current sheet, as described in Section 5.2.

During the plasmoid instability phase, the helium species molar fraction increases (from 6% to 10%) in the core of plasmoids, as shown in panel (F) of Figure 9). This separation process, also called chemical fractionation, occurs inside the plasmoids and remains even when the latter are advected along

the z -axis. This separation process occurs due to the ionization of the helium species during the instability phase.

At a later time of the plasmoid instability phase, the chemical fractionation process becomes stronger, leading to more helium species inside the current sheet that are advected toward outflow regions. This effect is illustrated in panel (I) of Figure 9. Indeed, an increase in the helium species, up to 12%, in the middle of the current sheet at $y = L_0/2$ and $z \in [0.4, 1.5]$ Mm is shown. Note that the fusion of plasmoids also leads to a large increase in helium abundance as we can see in the same figure, in the current sheet at $z = 2.9$ Mm.

To characterize the chemical fractionation in the outflows, the fluxes in number densities of helium and hydrogen species have been calculated and compared at the exhaust of the reconnection event until $t_{\text{end}} = 454$ s. These calculations have been performed at a fixed $z = 0.825$ Mm. For any species

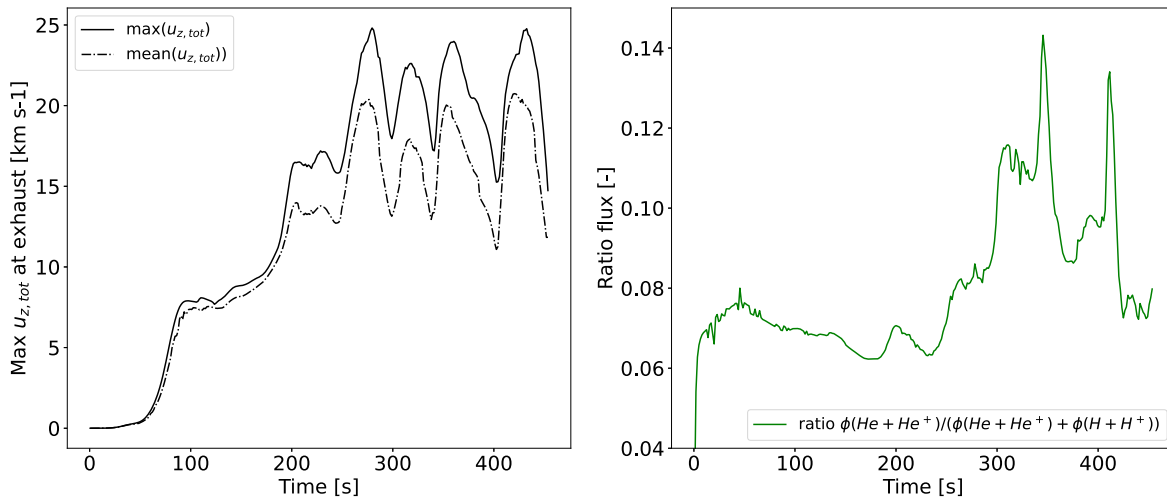


Figure 11. Distribution of the evolution in time of the maximum and mean total outflow velocities (left) and the ratio of fluxes $\phi(\text{He} + \text{He}^+)/(\phi(\text{He} + \text{He}^+) + \phi(\text{H} + \text{H}^+))$ (right) for the MFMS model at the exhaust. On the left figure, the solid and dashed black lines correspond to the maximum and mean total outflow velocities.

$\alpha\mathcal{I} \in \mathcal{M}$, its corresponding flux in number density is calculated as

$$\phi(\alpha\mathcal{I}) = dt dx \int_{l_y} [u_{z,\alpha\mathcal{I}} n_{\alpha\mathcal{I}}](y, z = 0.825 \text{ Mm}) dy, \quad (22)$$

where dx is the grid size in the x direction and set to one, l_y is the length in the y direction limited to the outflow region. We define the outflow regions as the FWHM of the maximum outflow at $z = 0.825 \text{ Mm}$. Similarly as the thickness of the current sheet in Section 5.1, this length has been calculated by locating the maximum outflow velocity at $z = 0.825 \text{ Mm}$. Then, we consider the termination of the exhaust at approximately 90% of this maximum in the y direction to estimate l_y .

Figure 11 shows the time evolution of the maximum and mean total outflow velocity (left) and the ratio of flux of helium species with respect to the flux of all species $\phi(\text{He} + \text{He}^+)/(\phi(\text{He} + \text{He}^+) + \phi(\text{H} + \text{H}^+))$ (right). In Figure 11, if the ratio is above 0.079 (corresponding to the initial total number density of helium species 7.9% shown in Table 1) means helium enrichment and, otherwise, hydrogen enrichment.

Our calculations show that during most of the reconnection process, the flux in the number density of the helium species represents 6%–8% of the total flux of all species, as shown in the bottom left panel of Figure 11. Helium is enhanced at the exhaust when the helium ionization starts at $t \approx 250 \text{ s}$ during the plasmoid instability regime. It increases the helium flux up to 14% of the total flux, as shown in the bottom left panel of Figure 11. These calculations are consistent with our figures presented in Figure 9. The helium enrichment in the outflows during the strongest flows and late-formed plasmoids also depends on the amount of helium species collected during the formation of plasmoids and the current sheet. In some localized events on the right-hand side of the reconnection, we found the opposite behavior when He has been previously deployed, and hydrogen is left in the latest plasmoids leading to the opposite, i.e., enrichment of hydrogen.

Note that, from $t \approx 250 \text{ s}$ to $t_{\text{end}} = 454 \text{ s}$, strong variations in the maximum and mean total outflow velocities at the exhaust appear, as shown in the top left of Figure 11 ranging between

15 and 24 km s^{-1} for the maximum outflow velocity. These peaks coincide with peaks in the flux of helium species with respect to the total flux, as shown in the bottom left of Figure 11. We note that the helium species are mostly ionized at the exhaust, as illustrated in Figure 8 on the right.

Taking the complexity of the chemical evolution into account, chromospheric reconnection may play a role in helium enrichment. In short, at the laminar phase, the ionization fraction for hydrogen is higher, and it is slowly expelled. At that time, outflows are relatively small. However, during the second phase, with stronger flows and plasmoids, the number of helium atoms is larger and helium is ionized due to the temperature increase, resulting in an enrichment of helium at the outflows. However, as mentioned above, in some locations on the right-hand side of the reconnection, stronger flows also could produce hydrogen enrichment depending on the history of the plasma evolution inside the current sheet, so care must be taken when interpreting these results.

6. Conclusions and Discussion

In order to study a magnetic reconnection event under upper-chromospheric conditions, we have focused on an MFMS MHD model and compared it with a TF MHD model using the Ebysus code. The MFMS model is an extension of the TF approach, generalized to any possible species with different ionization levels, considered as separate fluids and coupled altogether with collisions and ionization or recombination processes. Both models include anisotropic electron thermal conductivity and radiative losses. In this work, we have focused on two different mixtures: a helium–hydrogen mixture (MFMS model) \mathcal{M} and a hydrogen or two-fluid (TF model) mixture \mathcal{M}_{TF} . By doing so, our strategy allows the comparison of the classical two-fluid approach (see Leake et al. 2012, 2013; Murtas et al. 2021) with an MFMS approach and highlight the role of the helium species in a chromospheric reconnection event. Unlike previous studies of chromospheric magnetic reconnection from the literature (see Leake et al. 2012, 2013; Murtas et al. 2021), the collisional frequencies are not assumed to be constant but are calculated accurately based on a formalism with collision integrals consistent at the kinetic level

with the 13N moment model, as described in further detail in Wargnier et al. (2022).

For the two approaches, TF and MFMS, we have considered a perturbed Harris current sheet in upper-chromospheric conditions, inspired by Leake et al. (2012) and Leake & Linton (2013). We have compared and analyzed results in both cases at different levels: the evolution of the total current sheet, the velocity fields and decoupling of the particles, the composition and evolution of the ionization levels in the MFMS and TF models, and the main heating processes.

For both cases, we have two different phases: (1) a laminar phase where an elongated current sheet is formed and (2) a plasmoid instability phase where many plasmoids are formed and are advected from the middle of the reconnection region toward the outflow regions. Our calculations have shown that the evolution of the current sheet and the structure of the total velocity fields slightly differs between MFMS and TF. Indeed, in MFMS, the presence of helium species slightly slows the flow, leading to slightly smaller velocities in MFMS than in TF. Additionally, the average thickness of the current sheet and plasmoids is larger in MFMS than in TF while the average length of the current sheet is similar between the two.

During the laminar phase, outflow and inflow velocities are formed due to the Lorentz force generated by the initial structure of the magnetic field. In both MFMS and TF, velocities reach 20 km s^{-1} and 3.5 km s^{-1} in the z and y directions, respectively. In both directions, in the MFMS model, our calculations have shown that the drift velocity between H^+ and He is much higher than any other drift velocities. This decoupling is due to the fact that neutrals He decouples from H and H^+ when the thickness of the current sheet thins down to the order of the mean free path between He and H^+ or H, and neutral He atoms are not dragged into the current sheet as quickly as H and H^+ . The decoupling between neutral helium He and H or H^+ is higher than the decoupling between neutral hydrogen H and H^+ . This is attributed to the smaller collisional rate of He– H^+ or He–H interactions compared to that of H– H^+ interactions in upper-chromospheric conditions.

We refer to Wargnier et al. (2022) for further details about the magnitude of these collisional rates. The relatively large He and H^+ drift velocities in the MFMS model do not occur in the TF model as the latter considers only hydrogen species, i.e., H and H^+ .

During the plasmoid instability phase, the amplitude of all the drift velocities increases in both the MFMS and TF models. The amplitude of the drift velocity associated with He– H^+ interactions is the highest inside plasmoids. In the MFMS model, the drift between H and H^+ is stronger at the boundary of plasmoids and inside the current sheet, while it is approximately 3 times smaller and shows an oscillating pattern parallel to the current sheet in the TF model. In both the MFMS and TF models, the decoupling between H and H^+ occurs because the thickness of the current sheet continues to thin down to the order of the mean free path between H and H^+ , and neutral H does not collide enough with H^+ during the plasmoid instability phase, similarly to He– H^+ interactions in the MFMS model during the laminar phase. The amplitude of the drift between H and H^+ is smaller in the TF model than in the MFMS model—meaning that the collisional coupling is stronger in the TF model than in the MFMS model due to

the presence of the helium species, as described in further detail in Section 5.2.

In both models, the main heating processes are due to the drift velocities between any possible particles, also written as $Q_{aL,a'T}^{u,col}$. During the laminar phase, our calculations have shown that adding helium to the model allows to considerably increase the temperature of the plasma in the current sheet compared to the TF model. Inside the current sheet, the temperature is approximately 28,000 K in the MFMS model and 19,000 K in the TF model. In this context, a sufficient level of temperature is reached due to collisions associated with H– H^+ in the current sheet to ionize helium. Finally, collisions associated with He– He^+ and He– H^+ produce a small additional heating in the core of plasmoids and allow them to maintain the temperature level to 60,000 K whereas only 30,000 K is reached with the TF model. Note that, as the electrons are strongly coupled by collisions with H^+ species, the maximum electron temperature reached is also at 60,000 K.

In the MFMS approach, due to the weak coupling between neutral helium and other species, strong thermal decoupling effects have been obtained at a later time of the plasmoid instability phase. Our results have demonstrated that the temperature of neutral helium inside plasmoids can increase drastically up to 90,000 K while the temperatures of other species reach a maximum of 70,000 K. Note that a potential improvement of these models would be to include photo-ionization of helium species, as highlighted by Golding et al. (2014, 2016).

By combining a model where the collisional rates have been calculated accurately with an efficient numerical strategy, we have demonstrated that in upper-chromospheric magnetic reconnection the inclusion of helium species in the system allows for a considerable increase in the temperature of the plasma while the flows are weaker than those in a model where only hydrogen species are considered. This large increase in temperature compared to a classical two-fluid case is associated with a weak coupling between neutral helium and hydrogen that leads to a high energy release due to large drift velocities in the current sheet and inside plasmoids. In addition, during the plasmoid instability phase, inside the plasmoids, two efficient mechanisms can occur and allow an additional increase in temperature: the production of He^+ due to ionization and recombination processes and collisions with other species, and thermal decoupling effects, which can increase the temperature of neutral helium species locally. These mechanisms are able to easily increase the temperature of the plasma during the plasmoid instability regime of a magnetic reconnection event from upper-chromospheric temperatures (16,000 K) to transition region temperatures (90,000 K) on typical spatial and temporal scales of Megameters and minutes, respectively.

During the laminar phase, the total ionization level is much higher in the MFMS model (from 85% to 95%) than in the TF model (from 70% to 80%) due to the more efficient heating mechanisms in the former, as described previously, leading to higher temperatures in the current sheet giving rise to a large increase in the total ionization level, mostly populated by H^+ . During the plasmoid instability phase, in both the MFMS and TF models, the total ionization level increases drastically in the current sheet and plasmoids. In the MFMS model, both neutral hydrogen and helium species are ionizing; thus, the plasmoids and current sheet are mostly populated by H^+ and He^+ . In the

TF model, the total ionization level inside the plasmoids, mostly due to the presence of H^+ species, is slightly smaller than in the MFMS model and ranges from 80% to 98%.

Note that, at a later time of the plasmoid instability phase, chemical fractionation effects have been captured in the MFMS model. Indeed, as shown in Section 5.4, the helium and hydrogen species are separated inside the current sheet, characterized by an increase in the helium species (from 5% to 12%) and a decrease in the hydrogen species (from 98% to 89%), which are advected in the outflow directions, along the z -axis. During the plasmoid instability phase, the temperature increases inside the current sheet and results in the ionization of the helium species leading to helium species enrichment at the exhaust of the reconnection.

Our study suggests that reconnection could lead to an enrichment of helium during the strong outflow regimes under certain conditions. This mechanism, out of reach for the single-fluid or two-fluid MHD approaches, might explain the enhancement in the helium species observed at upper layers of the solar atmosphere associated to the switchbacks (Bale et al. 2021; Fargette et al. 2021) from the upper chromosphere. However, this analysis requires the inclusion of gravity. Similarly, intriguing observations of enhanced helium abundance in coronal mass ejections have been linked to reconnection events in the chromosphere (Fu et al. 2020). Our results suggest that, in the upper layer of the solar atmosphere, any event associated with a large variation or reconfiguration of the magnetic field could in principle release a sufficient level of energy to produce this chemical fractionation between the hydrogen and helium species while increasing the temperature of the plasma. However, these results have been performed under the following assumptions. A simplified model of the radiation has been considered, the effect of gravity and the Hall term have been neglected, and the spatial resolution does not fully resolve all the length scales associated with mean free paths of the MFMS and TF models. In particular, those involving electrons and some of the charged species. A simulation of a full stratified atmosphere with a helium–hydrogen mixture, including alpha particles, while guaranteeing that most of the mean free paths in that mixture are spatially resolved, would be necessary to further investigate this issue. Additionally, as described in Gudiksen et al. (2011), a more realistic model of the radiation coupled with Ebysus is required to better quantify the energy budgets in upper-chromospheric magnetic reconnection events.

We gratefully acknowledge support by NASA contracts, NNX17AD33G, 80NSSC18K1285, 80NSSC20K1272, and NNG09FA40C (IRIS), NSF contract AST1714955. Resources supporting this work were provided by the NASA High-End Computing (HEC) Program through the NASA Advanced Supercomputing (NAS) Division at Ames Research Center. The simulations have been run on clusters from the Notur project, and the Pleiades cluster through computing projects s1061, s2053, and s8305. We thankfully acknowledge the support of the Research Council of Norway through contract 230938/F50 and through grants of computing time from the Programme for Supercomputing.

Appendix A Definition of the MFMS Resistivity in the Small-drift-velocity Asymptotic Limit

By considering the definition of the electric field and electron velocity from Equations (12) and (14) it is possible to provide a new definition of the resistivity of the MFMS model in terms of the collision integrals $\Omega_{\epsilon, \alpha\mathcal{I}}^{1,1}(\mu_{\epsilon, \alpha\mathcal{I}})$, $\alpha\mathcal{I} \in \mathcal{H}$ following Wargnier et al. (2022). Indeed, assuming that the mass of the electrons is much smaller than the mass of any heavy particles, the collisional frequencies between ϵ and any $\alpha\mathcal{I} \in \mathcal{H}$ reads

$$\nu_{\epsilon, \alpha\mathcal{I}}^{\text{col}} = \frac{4}{3} \frac{m_{\epsilon, \alpha\mathcal{I}}}{m_{\epsilon}} n_{\alpha\mathcal{I}} |u_{\epsilon, \alpha\mathcal{I}}^{\text{th}}| \Omega_{\epsilon, \alpha\mathcal{I}}^{1,1}(\mu_{\epsilon, \alpha\mathcal{I}}) \approx \frac{4}{3} n_{\alpha\mathcal{I}} |u_{\epsilon}^{\text{th}}| \Omega_{\epsilon, \alpha\mathcal{I}}^{1,1}(\mu_{\epsilon}), \quad (\text{A1})$$

where the thermal speed is simply defined as $|u_{\epsilon}^{\text{th}}| = \sqrt{8/\pi\mu_{\epsilon}}$. If we consider the definition of Equation (A1) and the third term of Equation (12) we obtain

$$-\frac{1}{n_{\epsilon} q_{\epsilon}} \mathbf{R}_{\epsilon}^{\text{col}} = \frac{4}{3} \frac{m_{\epsilon}}{q_{\epsilon}^2 x_{\hat{x}}} \sum_{\alpha\mathcal{I} \in \mathcal{H}} x_{\alpha\mathcal{I}} \Omega_{\epsilon, \alpha\mathcal{I}}^{1,1}(\mu_{\epsilon}) \times \left[\sum_{\alpha'\mathcal{I}' \in \mathcal{H}} n_{\alpha'\mathcal{I}'} q_{\alpha'\mathcal{I}'} \mathbf{u}_{\alpha'\mathcal{I}'} - \mathbf{J} - n_{\epsilon} q_{\epsilon} \mathbf{u}_{\alpha\mathcal{I}} \right], \quad (\text{A2})$$

where $x_{\hat{x}} = n_{\epsilon}/(n_{\epsilon} + \sum_{\alpha\mathcal{I} \in \mathcal{H}} n_{\alpha\mathcal{I}})$ is the ionization fraction of the entire plasma, and $x_{\alpha\mathcal{I}} = n_{\alpha\mathcal{I}}/(n_{\epsilon} + \sum_{\alpha'\mathcal{I}' \in \mathcal{H}} n_{\alpha'\mathcal{I}'})$ is the molar fraction of particle $\alpha\mathcal{I} \in \mathcal{H}$. Equation (A2) can be interpreted as the resistive term of the MFMS model. In the limit where the drift velocities are smaller than the hydrodynamic velocity of the plasma or if the plasma is fully ionized or if the plasma is composed only of one type of ionized species, Equation (A2) simplifies to

$$\frac{1}{n_{\epsilon} q_{\epsilon}} \mathbf{R}_{\epsilon}^{\text{col}} \approx \left[\frac{4}{3} \frac{m_{\epsilon}}{q_{\epsilon}^2 x_{\hat{x}}} \sum_{\alpha\mathcal{I} \in \mathcal{H}} x_{\alpha\mathcal{I}} \Omega_{\epsilon, \alpha\mathcal{I}}^{1,1}(\mu_{\epsilon}) \right] \mathbf{J} = \eta \mathbf{J}, \quad (\text{A3})$$

where the resistivity is defined as $\eta = \frac{4}{3} \frac{m_{\epsilon}}{q_{\epsilon}^2 x_{\hat{x}}} \sum_{\alpha\mathcal{I} \in \mathcal{H}} x_{\alpha\mathcal{I}} \Omega_{\epsilon, \alpha\mathcal{I}}^{1,1}(\mu_{\epsilon})$. Therefore, we have been able to define the resistivity of the MFMS model in terms of collision integrals for any possible mixture valid in the asymptotic limit where the drift velocities are assumed to be much smaller than the hydrodynamic velocities of the MFMS plasma. Note that this resistivity coefficient is always true for the TF case based on \mathcal{M}_2 TF.

Appendix B Compact Form of the MFMS Governing Equations

The presented system (Equations (1), (4), (6), (7), and (13)) of the MFMS model can be rewritten in a compact form. By doing so, we can easily distinguish the nature of the different terms involved in the system. The system can be rewritten as

$$\begin{aligned} \partial_t U + \nabla \cdot F(U) + \nabla \cdot D(U, \nabla U) \\ = S^{\text{conv}}(U, \nabla U) + S^{\text{stiff}}(U), \end{aligned} \quad (\text{B1})$$

where $U \in \mathbb{R}^{5n_{\mathcal{I}}+4}$, $F(U) \in \mathbb{R}^{3 \times (5n_{\mathcal{I}}+4)}$, $D(U, \nabla U) \in \mathbb{R}^{3 \times (5n_{\mathcal{I}}+4)}$, $S^{\text{conv}}(U, \nabla U) \in \mathbb{R}^{5n_{\mathcal{I}}+4}$, and $S^{\text{stiff}}(U) \in \mathbb{R}^{5n_{\mathcal{I}}+4}$. These terms


read

$$\begin{aligned}
U &= ((\rho_{\alpha\mathcal{I}})_{\alpha\mathcal{I}\in\mathcal{H}}, (\rho_{\alpha\mathcal{I}}\mathbf{u}_{\alpha\mathcal{I}}^T)_{\alpha\mathcal{I}\in\mathcal{H}}, \\
&(e_{\alpha\mathcal{I}})_{\alpha\mathcal{I}\in\mathcal{H}}, e_e, \mathbf{B}^T)^T, \\
F(U) &= ((\rho_{\alpha\mathcal{I}}\mathbf{u}_{\alpha\mathcal{I}})_{\alpha\mathcal{I}\in\mathcal{H}}, (\rho_{\alpha\mathcal{I}}\mathbf{u}_{\alpha\mathcal{I}} \otimes \mathbf{u}_{\alpha\mathcal{I}} + P_{\alpha\mathcal{I}}\mathbb{I})_{\alpha\mathcal{I}\in\mathcal{H}}, \\
&(e_{\alpha\mathcal{I}}\mathbf{u}_{\alpha\mathcal{I}})_{\alpha\mathcal{I}\in\mathcal{H}}, e_e\mathbf{u}_e, \mathbb{I} \wedge (\mathbf{u}_e \wedge \mathbf{B}))^T, \\
D(U, \nabla U) &= (0_{n_{\mathcal{H}}}, 0_{3 \times n_{\mathcal{H}}}, 0_{n_{\mathcal{H}}}, \kappa_e \cdot \nabla k_B T_e, 0_3) \\
S^{\text{conv}}(U, \nabla U) &= \left(0_{n_{\mathcal{H}}}, \left(n_{\alpha\mathcal{I}} q_{\alpha\mathcal{I}} \left([\mathbf{u}_{\alpha\mathcal{I}} + \mathbf{u}_e] \wedge \mathbf{B} - \frac{\nabla P_e}{n_e q_e} \right) \right)_{\alpha\mathcal{I}\in\mathcal{H}}, \right. \\
&\left. - (P_{\alpha\mathcal{I}} \nabla \cdot \mathbf{u}_{\alpha\mathcal{I}})_{\alpha\mathcal{I}\in\mathcal{H}}, -P_e \nabla \cdot \mathbf{u}_e, -\nabla \wedge \left(\frac{1}{n_e q_e} \nabla P_e \right) \right) \\
S^{\text{stiff}}(U) &= ((m_{\alpha\mathcal{I}} \Gamma_{\alpha\mathcal{I}}^{\text{ion}} + m_{\alpha\mathcal{I}} \Gamma_{\alpha\mathcal{I}}^{\text{rec}})_{\alpha\mathcal{I}\in\mathcal{H}}, \\
&\left(\mathbf{R}_{\alpha\mathcal{I}}^{\text{ion}} + \mathbf{R}_{\alpha\mathcal{I}}^{\text{rec}} + \mathbf{R}_{\alpha\mathcal{I}}^{\text{col}} + \left[\frac{n_{\alpha\mathcal{I}} q_{\alpha\mathcal{I}}}{n_e q_e} \right] \mathbf{R}_e^{\text{col}} \right)_{\alpha\mathcal{I}\in\mathcal{H}}, \\
&(Q_{\alpha\mathcal{I}}^{\text{ion}} + Q_{\alpha\mathcal{I}}^{\text{rec}} + Q_{\alpha\mathcal{I}}^{\text{col}})_{\alpha\mathcal{I}\in\mathcal{H}}, Q_e^{\text{ion}} + Q_e^{\text{rec}} + Q_e^{\text{col}}, \nabla \wedge \left(\frac{\mathbf{R}_e^{\text{col}}}{n_e q_e} \right))
\end{aligned}$$

where U are the conservative variables of the system, F are the convective fluxes, D are the diffusive fluxes, κ_e is the anisotropic electron thermal conductivity, S^{conv} are the source terms that form part of the convective system, and S^{stiff} are the stiff source terms associated with collisions and ionization/recombination processes; $0_{n_{\mathcal{H}}}$ is a null vector of size $n_{\mathcal{H}}$, and \mathbb{I} is the identity matrix.

Note that in this system the only diffusive flux is the one associated with the Spitzer term in the equation of the thermal energy of the electrons. The source terms S^{conv} have characteristic timescales, which can be typically much larger than S^{stiff} . Indeed, S^{stiff} have timescales at the order of the collisional, ionization, and recombination rates between all particles $\alpha\mathcal{I} \in \mathcal{M}$. One can notice that the Lorentz force terms in the momentum equations have been split into two parts, one in the S^{conv} part and the other one in S^{stiff} . This is because the part of the Lorentz force as $\left[\frac{n_{\alpha\mathcal{I}} q_{\alpha\mathcal{I}}}{n_e q_e} \right] \mathbf{R}_e^{\text{col}}$ has a characteristic timescale, which is of the order of the collisional time between electrons and heavy particles, which can be much smaller than the other terms of the Lorentz force.

ORCID iDs

J. Martínez-Sykora  <https://orcid.org/0000-0002-0333-5717>
V. H. Hansteen  <https://orcid.org/0000-0003-0975-6659>
B. De Pontieu  <https://orcid.org/0000-0002-8370-952X>

References

- Abdulle, A., & Vilmart, G. 2013, *JCoPh*, **242**, 869
Aldrovandi, S. M. V., & Pequignot, D. 1973, *A&A*, **25**, 137
Alvarez Laguna, A., Lani, A., Deconinck, H., Mansour, N. N., & Poedts, S. 2016, *JCoPh*, **318**, 252
Asplund, M., Grevesse, N., Sauval, A. J., & Scott, P. 2009, *ARA&A*, **47**, 481
Bale, S. D., Horbury, T. S., Velli, M., et al. 2021, *ApJ*, **923**, 174
Ballester, J. L., Alexeev, I., Collados, M., et al. 2018, *SSRv*, **214**, 58
Bharti, L., Hirzberger, J., & Solanki, S. K. 2013, *A&A*, **552**, L1
Bhattacharjee, A., Huang, Y.-M., Yang, H., & Rogers, B. 2009, *PhPI*, **16**, 112102
Bhattacharjee, A., Sullivan, B., & Huang, Y.-M. 2010, *APS*, **52**, CP9
Brackbill, J. U., & Barnes, D. C. 1980, *JCoPh*, **35**, 426
Bruno, D., Catalfamo, C., Capitelli, M., et al. 2010, *PhPI*, **17**, 112315

- Cargill, P. 2013, *A&G*, **54**, 3.16
Cassak, P. A., Shay, M. A., & Drake, J. F. 2009, *PhPI*, **16**, 120702
Cook, A. W., & Cabot, W. H. 2005, *JCoPh*, **203**, 379
De Pontieu, B., McIntosh, S. W., Hansteen, V. H., & Schrijver, C. J. 2009, *ApJL*, **701**, L1
De Pontieu, B., Rouppe van der Voort, L., McIntosh, S. W., et al. 2014a, *Sci*, **346**, 315
De Pontieu, B., Title, A. M., Lemen, J. R., et al. 2014b, *SoPh*, **289**, 2733
Del Zanna, G., Dere, K. P., Young, P. R., Landi, E., & Mason, H. E. 2015, *A&A*, **582**, A56
Descombes, S., & Massot, M. 2004, *NuMat*, **97**, 667
Duarte, M., Descombes, S., Tenaud, C., Candel, S., & Massot, M. 2013, *CoFI*, **160**, 1083
Fargette, N., Lavraud, B., Rouillard, A. P., et al. 2021, *ApJ*, **919**, 96
Fu, H., Harrison, R. A., Davies, J. A., et al. 2020, *ApJL*, **900**, L18
Golding, T. P., Carlsson, M., & Leenaarts, J. 2014, *ApJ*, **784**, 30
Golding, T. P., Leenaarts, J., & Carlsson, M. 2016, *ApJ*, **817**, 125
Golding, T. P., Leenaarts, J., & Carlsson, M. 2017, *A&A*, **597**, A102
Gontikakis, C., Winebarger, A. R., & Patsourakos, S. 2013, *A&A*, **550**, A16
Gosling, J. 2007, *ApJL*, **671**, L73
Graille, B., Magin, T. E., & Massot, M. 2009, *Math. Models Methods Appl. Sci.*, **19**, 527
Gudiksens, B. V., Carlsson, M., Hansteen, V. H., et al. 2011, *A&A*, **531**, A154
Guo, L.-J., Pontieu, B. D., Huang, Y.-M., Peter, H., & Bhattacharjee, A. 2020, *ApJ*, **901**, 148
Hairer, E., & Wanner, G. 1996, *Solving Ordinary Differential Equations. II. Stiff and Differential-Algebraic Problems* (Berlin: Springer)
Hairer, E., & Wanner, G. 1999, *JCoAM*, **111**, 93
Hansteen, V., Ortiz, A., Archontis, V., et al. 2019, *A&A*, **626**, A33
Hansteen, V. H., Archontis, V., Pereira, T. M. D., et al. 2017, *ApJ*, **839**, 22
Hansteen, V. H., Leer, E., & Holzer, T. E. 1997, *ApJ*, **482**, 498
Huang, Y.-M., & Bhattacharjee, A. 2010, *PhPI*, **17**, 062104
Huang, Y.-M., & Bhattacharjee, A. 2016, *ApJ*, **818**, 20
Huang, Y.-M., Comisso, L., & Bhattacharjee, A. 2017, *ApJ*, **849**, 75
Hyman, J., Vichnevsky, R., & Stepleman, R. 1979, *Adv. Comp. Meth., PDE's-III*, 313
Janev, R., Harrison, M., & Drawin, H. 1989, *Nucl. Fusion*, **29**, 109
Judge, P. 2007, *The HAO Spectral Diagnostic Package for Emitted Radiation (HAOS-DIPER) Reference Guide v1.0*, NCAR/TN-473+STRUniversity Corporation for Atmospheric Research
Kasper, J. C., Abiad, R., Austin, G. W., et al. 2015, *SSRv*, **204**, 131
Khomenko, E., Collados, M., Díaz, A., & Vitas, N. 2014, *PhPI*, **21**, 092901
Khomenko, E., Vitas, N., Collados, M., & de Vicente, A. 2018, *A&A*, **618**, A87
Klimchuk, J. A. 2015, *RSPTA*, **373**, 20140256
Leake, J. E., & Arber, T. D. 2006, *A&A*, **450**, 805
Leake, J. E., Daldorff, L. K. S., & Klimchuk, J. A. 2020, *ApJ*, **891**, 62
Leake, J. E., & Linton, M. G. 2013, *ApJ*, **764**, 54
Leake, J. E., Lukin, V. S., & Linton, M. G. 2013, *PhPI*, **20**, 061202
Leake, J. E., Lukin, V. S., Linton, M. G., & Meier, E. T. 2012, *ApJ*, **760**, 109
Loureiro, N. F., Cowley, S. C., Dorland, W. D., Haines, M. G., & Schekochihin, A. A. 2005, *PhRvL*, **95**, 235003
Loureiro, N. F., & Uzdensky, D. A. 2015, *PFCF*, **58**, 014021
Martínez-Sykora, J., Moreno-Insertis, F., & Cheung, M. C. M. 2015, *ApJ*, **814**, 2
Martínez-Sykora, J., Szydlarski, M., Hansteen, V. H., & Pontieu, B. D. 2020, *ApJ*, **900**, 101
Murtas, G., Hillier, A., & Snow, B. 2021, *PhPI*, **28**, 032901
Ni, L., Germaschewski, K., Huang, Y.-M., et al. 2010, *PhPI*, **17**, 052109
Ni, L., Ji, H., Murphy, N. A., & Jara-Almonte, J. 2020, *RSPSA*, **476**, 20190867
Ni, L., Lin, J., & Murphy, N. A. 2013, *PhPI*, **20**, 061206
Ni, L., & Lukin, V. S. 2018, *ApJ*, **868**, 144
Ni, L., Ziegler, U., Huang, Y.-M., Lin, J., & Mei, Z. 2012, *PhPI*, **19**, 072902
Niedziela, R., Murawski, K., & Poedts, S. 2021, *A&A*, **652**, A124
Nordlund, Å. 1982, *A&A*, **107**, 1
Nordlund, D., Martínez-Sykora, J., Moreno-Insertis, F., & Rouppe van der Voort, L. 2017, *ApJ*, **850**, 153
Parker, E. N. 1955, *ApJ*, **122**, 293
Parker, E. N. 1963, *ApJS*, **8**, 177
Pelekhatu, M., Murawski, K., & Poedts, S. 2021, *A&A*, **652**, A114
Peter, H., Tian, H., Curdt, W., et al. 2014, *Sci*, **346**, 1255726
Popescu Braileanu, B., Lukin, V. S., Khomenko, E., & de Vicente, Á. 2019, *A&A*, **627**, A25
Pucci, F., Singh, K. A. P., Tenerani, A., & Velli, M. 2020a, *ApJL*, **903**, L19
Pucci, F., Velli, M., Shi, C., et al. 2020b, *JPhPh*, **86**, 535860601
Rempel, M. 2016, *ApJ*, **834**, 10

- Rempel, M., & Przybylski, D. 2021, *ApJ*, **923**, 79
- Roupe van der Voort, L., De Pontieu, B., Scharmer, G. B., et al. 2017, *ApJL*, **851**, L6
- Soler, R., & Ballester, J. L. 2022, *FrASS*, **9**, 789083
- Spitzer, L. 1956, *Physics of Fully Ionized Gases* (New York: Interscience)
- Steinolfson, R. S., & Hoven, G. V. 1984, *PhFI*, **27**, 1207
- Sweet, P. A. 1958, in *IAU Symp. 6, Electromagnetic Phenomena in Cosmical Physics*, ed. B. Lehnert (Cambridge: Cambridge Univ. Press), 123
- Ugai, M. 1995, *PhPI*, **2**, 388
- Vernazza, J. E., Avrett, E. H., & Loeser, R. 1981, *ApJS*, **45**, 635
- Vernazza, J. E., & Mason, H. E. 1978, *ApJ*, **226**, 720
- Vranjes, J., & Poedts, S. 2009, *MNRAS*, **398**, 918
- Wargnier, Q. 2019, PhD thesis, CMAP, Ecole Polytechnique, <https://hal.science/tel-02500745v1>
- Wargnier, Q., Laguna, A. A., Kestener, P., et al. 2018, *JPhCS*, **1125**, 012021
- Wargnier, Q. M., Martínez-Sykora, J., Hansteen, V. H., & Pontieu, B. D. 2022, *ApJ*, **933**, 205
- Wilkins, M. L. 1980, *JCoPh*, **36**, 281
- Wójcik, D., Kúzma, B., Murawski, K., & Musielak, Z. 2020, *A&A*, **635**, A28
- Woolley, T., Matteini, L., McManus, M. D., et al. 2021, *MNRAS*, **508**, 236
- Young, P. R. 2018, *ApJ*, **855**, 15
- Zhdanov, V. 2002, *Transport Processes in Multicomponent Plasma* (London: Taylor & Francis)
- Zweibel, E. G., Lawrence, E., Yoo, J., et al. 2011, *PhPI*, **18**, 111211